CHALMERS

A CFD analysis of H_2SO_4 assisted alkali chloride sulfation in waste incineration

Master's thesis in:
Innovative and Sustainable Chemical Engineering
Sustainable Energy Systems

VIDAR AHLBERGER
SEBASTIAN SUNDELL

Department of Chemistry and Chemical Engineering
CHALMERS UNIVERSITY OF TECHNOLOGY
Gothenburg, Sweden 2019

Master's thesis, 2019

A CFD analysis of H_2SO_4 assisted alkali chloride sulfation in waste incineration

VIDAR AHLBERGER
SEBASTIAN SUNDELL

CHALMERS
UNIVERSITY OF TECHNOLOGY

Department of Chemistry and Chemical Engineering
Chalmers University of Technology
Gothenburg, Sweden 2019

A CFD analysis of H_2SO_4 assisted alkali chloride sulfation in waste incineration
VIDAR AHLBERGER
SEBASTIAN SUNDELL

Supervisor: Sven Andersson, Department of Chemistry and Chemical Engineering
Advisor: Thomas Allgurén, Department of Space, Earth and Environment
Examiner: Ronnie Andersson, Department of Chemistry and Chemical Engineering

Master's Thesis 2019
Department of Chemistry and Chemical Engineering
Division of Chemical Engineering
Chalmers University of Technology
SE-412 96 Gothenburg
Telephone +46 31 772 1000

Typeset in LaTeX
Gothenburg, Sweden 2019

A CFD analysis of H_2SO_4 assisted alkali chloride sulfation in waste incineration

VIDAR AHLBERGER
SEBASTIAN SUNDELL
Department of Chemistry and Chemical Engineering
Chalmers University of Technology

Abstract

Sulfur recirculation is a new technology for the reduction of alkali chlorides and dioxins in waste-to-energy plants. With sulfur recirculation, the high temperature corrosion caused by the alkali chlorides is reduced, which enables higher steam temperatures and thereby higher electrical efficiency. In this thesis work, a CFD analysis of sulfuric acid assisted alkali chloride sulfation in a waste incineration boiler has been done using ANSYS Fluent 18.0. The aim of this work was to gain a greater understanding of the sulfation process and thereby allow for optimisation and improvement. A validated temperature and flow field of the boiler from a previous work was used as a starting point. The first thing added to the simulation was the vaporisation of a sulfuric acid spray using a Lagrangian framework with discrete random walk and a multicomponent vaporisation model. A reduced chemical mechanism was required to simulate the sulfation in CFD for it to be computationally feasible to run. A gas phase kinetic model used in the previous work to predict the sulfation in waste-to-energy boilers was reduced from 288 reactions and 72 species to 90 reactions and 28 species. This mechanism was then simulated together with the eddy dissipation concept turbulent mixing model and gave results that greatly overpredicted the sulfation rate and underpredicted the conversion of SO_3 to SO_2. Modifications to the boundary conditions in order to achieve greater reaction rates with radical generating CO and H_2 were made. These modifications were based on previous work where additions of CO were made to increase the amount of radicals in the system. This proved beneficial for the SO_3 conversion; however the conversion was still much lower than the measured plant data. A second global reaction mechanism was therefore developed with least square minimization against data from a 1D simulation in CHEMKIN. This mechanism was also run in CFD with the eddy dissipation turbulent mixing model, which more correctly predicted the SO_3 conversion, while the sulfation was still overpredicted. However, there could be ways of improving this model. Suggestions for future work would be accounting for interactions with fly ash or evaluating other kinetic models.

Keywords: sulfur recirculation, waste-to-energy, waste incineration, computational fluid dynamics, CFD.

Acknowledgements

We would like to thank both our supervisor and examiner, Sven Andersson and Ronnie Andersson for all the help and support during the project. We would also like to thank Thomas Allgurén for helping us with the chemistry.

Vidar Ahlberger and Sebastian Sundell, Gothenburg, June 2019

Contents

Nomenclature

Abbreviations

B&W	Babcock & Wilcox Vølund AB
CFD	Computational Fluid dynamics
DO	Discrete Ordinates
DoS	Degree of Sulfation
DPM	Discrete Phase Modelling
DRG	Directed Relation Graph
DRGEP	Directed Relation Graph with Error Propagation
DRW	Discrete Random Walk
ED	Eddy Dissipation
EDC	Eddy Dissipation Concept
ESP	Electrostatic precipitator
ISAT	In-Situ Adaptive Tabulation
KIT	Karlsruhe Institute of Technology
MSW	Municipal Solid Waste
NP	Parcel particle number
PFR	Plug flow reactor
ppm	Parts per million (by volume)
PSR	Perfectly stirred reactor, either a 0D tank- or a 1D batch reactor
UDF	User defined function
WTE	Waste-to-Energy

Latin variables

$\dot{m}$	Mass flow rate	$[kgs^{-1}]$
$\hat{R}_i$	Kinetic rate for species i	$[kmolm^{-3}s^{-1}]$
$\vec{r}$	Position vector	$[m]$
$\vec{s}$	Direction vector	(unit vector)[-]
$\vec{s}'$	Scattering direction vector	(unit vector)[-]
A	Pre-exponential factor	(Depends on reaction order)
a	Absorption coefficient	$[m^{-1}]$
A_p	Particle surface area	$[m^2]$
B_{mi}	Spalding mass number for species i	[-]
B_{Ti}	Spalding temperature number for species i	[-]
C_D	Drag coefficient	[-]
C_j	Inlet concentration of species j	$[kmolm^{-3}]$
C_L	DRW constant	[-]

c_p	Specific heat	$[Jkg^{-1}K]$
$C_{i\infty}$	Local bulk concentration of species i	$[kmolm^{-3}]$
C_{is}	Surface concentration of species i	$[kmolm^{-3}]$
d_p	Particle diameter	$[m]$
D_t	Effective turbulent diffusivity	$[m^2s^{-1}]$
$D_{i,m}$	Laminar diffusivity of species i	$[m^2s^{-1}]$
E_a	Activation energy	$[Jkmol^{-1}]$
h	Heat transfer coefficient	$[Wm^{-2}K^{-1}]$
$h_{vap,i}$	Heat of vaporisation for species i	$[Jkg^{-1}]$
I	Radiative intensity	$[Wm^{-2}(sr)^{-1}]$
k	Turbulent kinetic energy	$[m^2s^{-2}]$
k_b	Reverse reaction rate constant	(Depends on reaction order)
k_f	Forward reaction rate constant	(Depends on reaction order)
k_{ci}	Mass transfer coefficient of species i	$[ms^{-1}]$
L	Characteristic length	$[m]$
m_i	Mass of species i in a particle	$[kg]$
m_p	Discrete particle mass	$[kg]$
$M_{w,i}$	Molar mass of species i	$[kg(kmol)^{-1}]$
n	Refractive index	[-]
R_i	Apparent source term for species i	$[kgm^{-3}s^{-1}]$
T	Local temperature	$[K]$
T_p	Particle temperature	$[K]$
T_∞	Fluid temperature	$[K]$
u_p	Discrete particle velocity	$[ms^{-1}]$
v	Velocity	$[ms^{-1}]$
x_i	Mass fraction of species i in the droplet	[-]
Y_i	Bulk mass fraction of species i	[-]
Y_i^*	Fine scale mass fraction of species i	[-]
Y_P	Product mass fraction in the ED model	[-]
Y_R	Reactant mass fraction in the ED model	[-]
A,B	Empirical constants in the ED model	[-]
Oh= $\frac{\mu}{\sqrt{\rho\sigma L}}$	Ohnesorge number, a measure of viscous forces to inertial and surface tension forces	[-]
Re= $\frac{\rho v L}{\mu}$	Reynolds number, a measure of inertial to viscous forces	[-]
Sc= $\frac{\mu}{\rho D}$	Schmidt number, a measure of momentum transport to molecular transport	[-]
$\mathrm{Sc}_t = \frac{\mu_t}{\rho D_t}$	Turbulent Schmidt number, a measure of momentum diffusivity to mass diffusivity in turbulent flows	[-]
Sh= $\frac{k_c L}{D}$	Sherwood number, a measure of convective mass transfer to diffusive mass transfer	[-]
We= $\frac{\rho v L}{\sigma}$	Weber number, a measure of inertial to surface tension forces	[-]

Greek variables

β	Reaction rate temperature exponent	[-]
ϵ_p	Particle emissivity	[-]

$\eta_j^{''}$	Rate exponent of product species j	[-]
$\eta_j^{'}$	Rate exponent of reactant species j	[-]
Γ	Net effect of third bodies on reaction rate	[-]
λ	Thermal conductivity	$[Wm^{-1}K^{-1}]$
μ	Dynamic viscosity	$[Pas]$
μ_t	Turbulent viscosity	$[Pas]$
ν	Kinematic viscosity	$[m^2s^{-1}]$
$\nu_i^{''}$	Product stoichiometric coefficient	[-]
$\nu_i^{'}$	Reactant stoichiometric coefficient	[-]
Ω	Solid angle	$[sr]$
Φ	Scattering phase function	[-]
ρ	Density	$[kgm^{-3}]$
σ	Surface tension	$[Nm^{-1}]$
σ_B	Boltzmann's constant	$[m^2kgs^{-2}K^{-1}]$
σ_s	Scattering coefficient	$[m^{-1}]$
$\tau*$	Turbulent fine scale reaction time	$[s]$
$\Theta_R = (\frac{\int_0^{4\pi} I d\Omega}{4\sigma_B})^{1/4}$	Radiation temperature	$[K]$
ε	Turbulent dissipation rate	$[m^2s^{-3}]$
ξ	Normally distributed random number in DRW	[-]
ξ^*	Length scale of the turbulent fine structures	[-]

1
Introduction

1.1 Background

As society attempts to move towards a sustainable economy the need for emission reduction is only increasing. One industry where this is very much the case is waste combustion which is in turn especially relevant in the Nordic region with its many waste combustion facilities. The reason for this is that the flue gases contain potentially destructive compounds for the environment. This means that for any waste combustion process to follow emissions standards, an extensive after-treatment system is required. The compounds to be removed are, among others, dioxins, hydrochloric acid and alkali chloride salts. The first is carcinogenic whilst the latter pose major corrosion problems in the boiler, limiting the maximum flue gas temperature. This limits the electrical efficiency of the plant and reduces the lifetime of the boiler equipment [1].

A recently developed method of reducing these substances is through the use of sulfur recirculation in the boiler. The point of recirculating the sulfur is to increase the amount of sulfur compared to chlorine in the flue gas which is advantageous for several reasons. The two primary advantages are the reduced amount of corrosion caused by the alkali chlorides and a reduced amount of formed dioxins. The sulfur recirculation technology was invented by Hans Hunsinger at KIT for which Babcock & Wilcox Vølund AB (B&W) have a world-wide exclusive license. The essence of the technology is using the naturally present sulfur in the flue gas and absorbing it in hydrogen peroxide, forming a sulfuric acid solution. This solution can then be injected into the furnace where the sulfuric acid decomposes into sulfur trioxide and sulfur dioxide. The sulfur dioxide and -trioxide react with the alkali chlorides, forming sulfates. The sulfates, in comparison to the chlorides, are less sticky and corrosive. A schematic representation of this system can be seen in Figure 1.1 [1, 2].

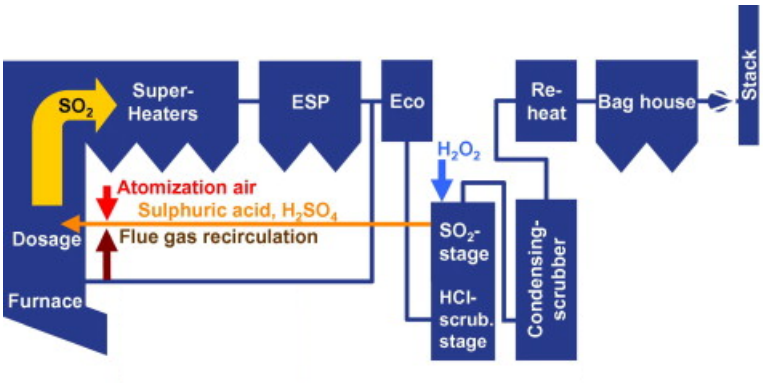

Figure 1.1: Schematic representation of Babcock & Wilcox Vølund AB's Sulfur Recirculation process [1].

This system has been tested at the Renova Sävenäs Waste-to-Energy (WTE) plant in Gothenburg and permanently installed at the WTE plant in the Måbjerg Energy Center in Holstebro, Denmark. With sulfur recirculation, the rate of corrosion decreased by 60-90 % and the flue gas dioxin concentration decreased by approximately 25 % in comparison to without sulfur recirculation [2].

1.2 Aim

The aim of this master thesis is to develop a model for the alkali sulfation process that is consistent with measured plant data. The aim is divided into the following objectives:

- Modify an existing CFD model of the Renova boiler for the inclusion of sulfuric spray.
- Formulate relevant models for liquid spray evaporation, mixing and reaction with alkali chlorides, and implement them in the CFD model.
- Validate the CFD model against experimental results from the actual process.

1.3 Limitations

The work is limited to the modelling of the reactions involving sulfuric acid and alkali chlorides in the boiler. Additions of CO and H_2 oxidation are made in some cases but the combustion is not modelled. A boiler CAD model and a solution for the flow and energy developed by Sundborg and Tärnåsen is used as a basis for the CFD simulations [3]. In terms of operating conditions, one case from the work of Sundborg and Tärnåsen is modelled.

2
Theory

2.1 Waste combustion

Combustion of municipal solid waste (MSW) is usually done in a grate fired furnace, as it handles the heterogeneous fuel well. In figure 2.1, a schematic of a grate fired furnace is shown. Before entering, the fuel is mixed as much as possible in order to homogenise the waste with respect to energy content and composition. The moving grate transports the fuel, where primary air, usually pre-heated, enters from below and combustion occurs. By introducing secondary air, a swirl above the fuel is generated, enhancing the mixing and combustion. The flue gas temperature after combustion may be between 800 and 1450 °C. If there is complete combustion in the furnace, only ash should be left. The ash can be either bottom ash or fly ash, where the fly ash leaves the flame with the flue gas and is separated in the flue gas treatment system [4].

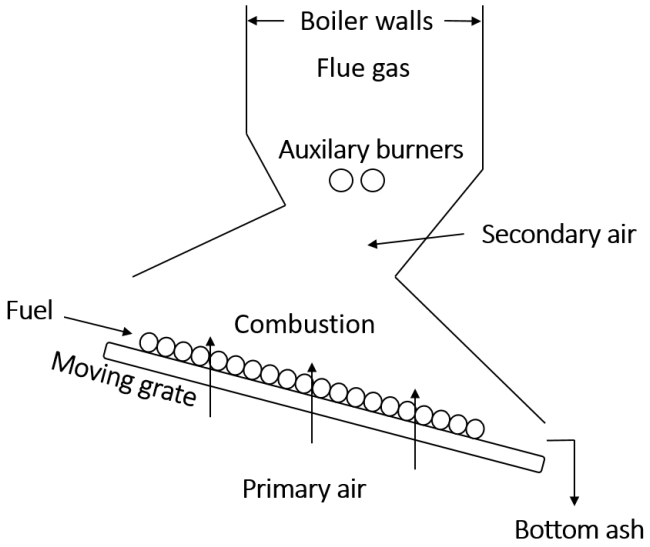

Figure 2.1: A grate fired furnace.

2.1.1 Chemical composition of the fuel and flue gas

MSW is highly heterogeneous and its chemical composition varies from combustion to combustion. Essentially, the main components are organic substances, minerals, metals and water [4]. With respect to chemical composition, the content of alkali and chlorine are higher in comparison to coal. By alkali the main constituents are Na, K and Ca [5]. The content of sulfur is slightly lower. Averaged on a dry basis, chlorine and sulfur comprise 0.73 % and 0.24 % of the MSW. The moisture content may be 25-85 % on a wet basis [1, 4, 6].

In the flue gas, the main components are N_2, CO_2, H_2O and O_2. To a lesser extent, in the ppm range, species such as SO_2, HCl and its alkali salts are present [7]. Only a few percent of the sulfur present is SO_3 [1]. The alkali chloride concentration can be several 100 ppm [3]. In table 2.1 the flue gas composition in a waste incinerator is presented.

Table 2.1: Chemical composition of the flue gas in a waste incinerator before the flue gas treatment [7].

Species	Value
N_2	balance vol%
CO_2	6-12 vol%
H_2O	10-18 vol%
O_2	7-14 vol%
CO	0.001-0.06 vol%
SO_2	200-1500 ppmw
HCl	400-3000 ppmw

2.2 Alkali chloride sulfation

Due to the high concentration of alkali chlorides in waste, there is a high rate of corrosion in the superheater section of the boiler. If alkali chlorides instead are sulfated, which is done by replacing the chloride ion in the salt by a sulfate ion, the level of corrosion can be reduced [1]. The alkali chlorides that are deemed to be of significance in the sulfur recirculation process are $NaCl$ and KCl. $CaCl_2$ is less corrosive and is rapidly converted to CaO at 600 °C [5]. Hence, $CaCl_2$ should not be of importance since the temperature in the furnace region, 800-1450 °C, means most if not all $CaCl_2$ is rapidly converted into CaO.

2.2.1 Detailed chemical kinetic model of the sulfation

An accurate model of the sulfation process requires detailed information about the chemical kinetics involved as to predict the rate of sulfation. Such detailed chemical kinetics models for the gas phase reactions have been produced by Mortensen et al., Hindiyarti et al. and Glarborg et al. [8, 9, 10].

The model by Hindiyarti et al. expands on the model of Glarborg et al. by adding the species $KHSO_3$ and KSO_4 and by using updated mechanisms for SO_2 oxidation. The model is partly based on experimental work on alkali sulfation by SO_2 in flow reactors and quantum chemistry computations. As such, the thermodynamic and kinetic properties of the alkali species have been computed based on quantum chemistry theory. In addition, kinetic parameters for the $H/S/O$ subset have been partially derived by ab initio methods as well as experimental work.

The model is consistent with observed experimental results but according to the authors, additional experimental work is needed to understand the fundamentals of sulfate aerosol formation [8]. The overall sulfation process reactions modelled are only the homogeneous gas phase reactions since it is assumed that the heterogenous reaction with solid phase alkali chlorides is much slower and can be neglected [11, 12].

MSW usually contains less potassium relative to sodium but the kinetics of sodium are less investigated [3, 8]. However, the chemistry of these species are very similar; therefore it was determined to let K represent all the alkali species. This was also done by Sundborg and Tärnåsen, which forms the basis of this work [3]. This simplifies the mechanism considerably, where 18 Na species and 65 reactions are removed.

There are a number of reaction pathways through which the sulfation occurs. Direct reactions between SO_2 and SO_3 with the alkali species can occur, as given by reactions 2.1-2.3.

$$SO_3 + KOH(+M) \Longleftrightarrow KHSO_4(+M) \tag{2.1}$$
$$SO_3 + KCl(+M) \Longleftrightarrow KSO_3Cl(+M) \tag{2.2}$$
$$K + SO_2 \Longleftrightarrow KSO_2 \tag{2.3}$$

Another important reaction in the kinetics is the conversion of SO_3 into SO_2. This can occur directly through reactions with oxygen radicals, hydroxyl radicals or hydrogen radicals, see reactions 2.4-2.6.

$$SO_3 + O \Longleftrightarrow SO_2 + O_2 \tag{2.4}$$
$$SO_3 + OH \Longleftrightarrow SO_2 + HO_2 \tag{2.5}$$
$$SO_3 + H \Longleftrightarrow SO_2 + OH \tag{2.6}$$

This conversion also occurs indirectly through an intermediary, $HOSO_2$, where reactions with radicals occur in two steps, see reactions 2.7-2.11.

$$SO_3 + H \Longleftrightarrow HOSO_2 \tag{2.7}$$
$$HOSO_2 + H \Longleftrightarrow SO_2 + H_2O \tag{2.8}$$
$$SO_3 + OH \Longleftrightarrow HOSO_2 + O \tag{2.9}$$
$$SO_3 + H_2O \Longleftrightarrow HOSO_2 + OH \tag{2.10}$$
$$HO_2 + SO_3 \Longleftrightarrow HOSO_2 + O_2 \tag{2.11}$$

The sulfated potassium species react to form K_2SO_4 mainly through reactions 2.12 and 2.13. The formed K_2SO_4 condenses as per reaction 2.14. In addition to the solid K_2SO_4, the condensed inert form of KCl is also included in the model.

$$KSO_3Cl + H_2O \Longleftrightarrow KHSO_4 + HCl \tag{2.12}$$
$$KHSO_4 + KCl \Longleftrightarrow K_2SO_4 + HCl \tag{2.13}$$
$$2K_2SO_4(g) \Longleftrightarrow 2K_2SO_4(s) \tag{2.14}$$

2.2.2 SO_2-SO_3 chemistry

The SO_2-SO_3 equilibrium is of importance for the sulfation process because sulfation through reactions with SO_3 is faster compared to reactions with SO_2. This means that a prediction of the SO_3-SO_2 ratio is necessary for a prediction of the sulfation. In the operating range of the boiler, 800-1500 K, the thermodynamically favoured form is that of SO_2 as shown in figure 2.2.

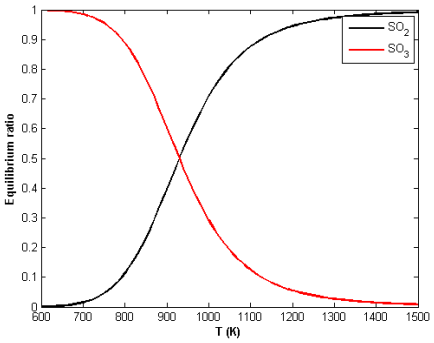

Figure 2.2: SO_2/SO_3 equilibrium based on the data from Hindiyarti et al. at flue gas conditions [8].

However, as described by Jørgensen, Livbjerg and Glarborg, the oxidation of SO_2 can be enhanced with the presence of water [13]. This is due to water vapour contributing to the O/H-radical pool, where the reactions 2.4-2.11 in section 2.2.1, involving SO_2/SO_3 interconversion, are affected. The effect of water vapour on the the conversion of SO_3 to SO_2 can be observed in figure 2.3. According to Hindiyarti, Glarborg and Marshall the reaction deemed to be of importance for the consumption of SO_3 is 2.6 whilst 2.4 is of less importance [14].

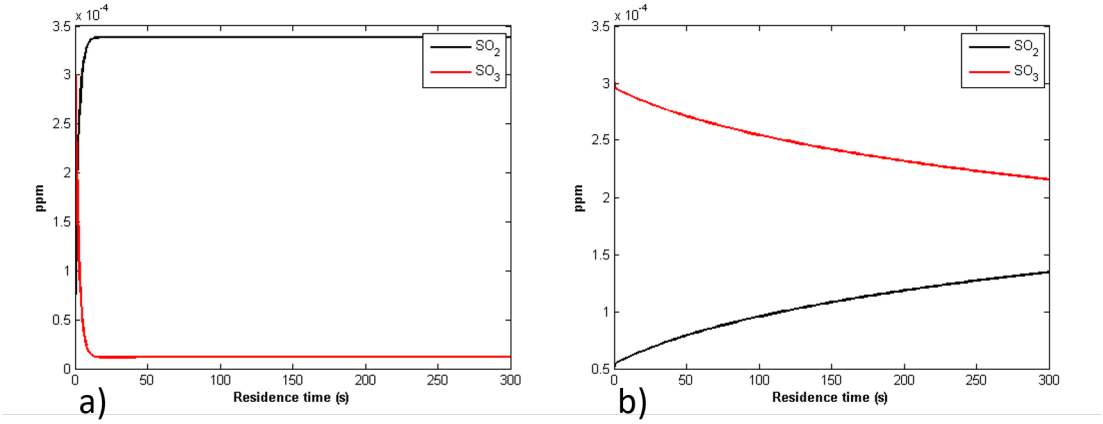

Figure 2.3: Two separate concentration profiles of SO_3 and SO_2 in a batch reactor at 1273 K with flue gas. Injected SO_3 is 300 ppm. The conditions are equivalent to those at the height of sulfur injection. a) water vapour present and b) no water vapour. CHEMKIN simulations based on the chemical mechanism by Hindiyarti et al. [8].

It has also been reported that the SO_2/SO_3 interconversion is affected by the presence of metal deposits, such as iron oxide from boiler walls or CaO in fly ash [8]. In a study conducted by Glarborg et al., it was showed in a laminar flow reactor at combustion conditions that iron oxide acts as a strong catalyzing agent. The homogeneous oxidation of SO_2 to SO_3 was found to be very slow, in comparison to the heterogeneous oxidation with iron oxide [13]. Metals acting as catalysts for SO_2 oxidation has been reported in earlier literature as well [8].

2.2.3 DRGEP

DRGEP stands for Directed Relation Graph with Error Propagation and is a method for reducing a chemical mechanism. It is an extension of DRG but both methods work similarly. The essence of the methods is to construct graphs based on the strength between the species. This strength is defined as the error if e.g. species C were to be removed from the mechanism and to what extent this removal has on the production rate of species A [15, 16]. The difference between the methods is the definition of the error. In short, DRGEP evaluates the indirect impact species C has on the production rate of A through an intermediate B. By removing species C from the mechanism, the error in comparison to if it were directly interacting with species A is damped, as it propagates from A through B to C [17]. In DRG, an indirect interaction between two species would be the treated the same as a direct interaction. By the DRGEP definition of the error, it has been shown that the number of species in a reduced mechanism can be removed by up to 10 % in comparison to DRG [18].

2.3 The Renova boiler

The master thesis is based on the previous CFD model of the Renova boiler provided by Sundborg and Tärnåsen [3]. The model has been modified with six spray injectors. The boiler is shown in figure 2.4. In the figure, one side of the boiler is shown with three injection points. These injectors are equally spaced with a spacing of 1.3 m. The other injectors are placed on the opposite side, with the exact same spacing.

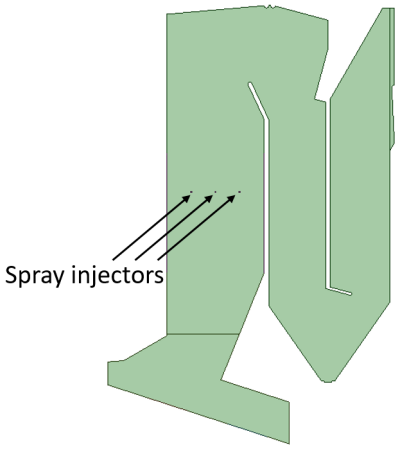

Figure 2.4: The boiler used in the CFD simulations with marked injection points.

2.3.1 Sulfuric acid injectors

The nozzle is a two-phase nozzle with liquid sulfuric acid, which is atomized into droplets by pressurized air as shown in figure 2.5. The spray nozzles are placed in recirculated flue gas nozzles in order to improve mixing into the flue gas. With all six injectors included and assuming perfectly mixed in the flue gas, this corresponds to a dosage of 274 ppm SO_3.

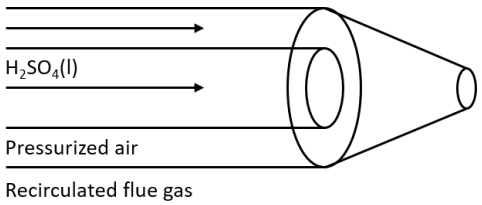

Figure 2.5: A simple schematic of the two-phase nozzle.

2.3.2 Validation

In order to validate that the CFD model physically represents the conditions in the boiler, the simulated results must be compared to validation data. The validation data is based on the experimental work of Andersson et al. [1, 19] and is found in table A.1, Appendix A.2. From the table the concentrations of SO_2, SO_3 and CO and the mass ratio SO_3/SO_2 are valid downstream of the boiler. The expected degree of sulfation (DoS) is based on the calculations of Sundborg and Tärnåsen. In addition, the amount of fly ash in the flue gas is 5 g/Nm^3 dry gas and the SO_2 outlet concentration without sulfur recirculation is approximately 50 ppm [3, 19].

2.4 Discrete Ordinates

Characteristic temperatures in the modelled boiler are 800-1500 K, which means that heat is to a great extent transported by radiation. Therefore, an accurate model for radiative heat transfer model must be applied. The discrete ordinates model accomplishes this by discretizing the geometry in directions, $\vec{s}$, along two spherical angles, ϕ and θ. These are split into into N_ϕ and N_θ number of parts respectively giving $8 \cdot N_\phi \cdot N_\theta$ number of directions. In each of these directions the total radiative heat transfer equation (2.15) is solved [20].

$$\nabla \cdot (I(\vec{r}, \vec{s})) + (a + \sigma_s) I(\vec{r}, \vec{s}) = an^2 \frac{\sigma_B T^4}{\pi} + \frac{\sigma_s}{4\pi} \int_0^{4\pi} I(\vec{r}, \vec{s}') \Phi(\vec{s} \cdot \vec{s}') d\Omega' \qquad (2.15)$$

The first term on the left is the change in radiation intensity I at a point $\vec{r}$ in the direction $\vec{s}$, followed by the gas absorption and outscattering of radiation intensity. From left to right on the right side of the equation, is the gas emission and inscattering [21].

A major problem in the discrete ordinates model is that the fluid equations are solved in parallel using arbitrary finite control volumes. This means that the edges of the cells are usually not aligned with the directions that the radiation is divided into. This is called control angle overhang, which means that it becomes difficult to determine whether the local radiation intensity is leaving or entering a cell. A solution to this problem is pixellating the overhang into smaller segments and as long as the pixellation is fine enough the overhang is accounted for without significant errors [20].

2.5 Droplet modelling

The injection of sulfuric acid into the system and the vaporisation of droplets is modelled by Discrete Phase Modelling (DPM) in Fluent. This is also known as

Lagrangian Particle Tracking (LPT), where each individual droplet is tracked in a Lagrangian, discrete reference frame. The individual droplets move through and interact with the continuous fluid, the flue gas, which is described by an Eulerian framework.

2.5.1 Discrete tracking

The velocity and position of the droplets is calculated by the equation of motion. Choosing the correct set of forces to include in this equation is often critical for an accurate simulation.

The two forces acting on the droplets deemed to be of most importance are the drag and the gravity. The gravity is modelled using a gravitational constant of 9.81 m/s^2 while the drag is modelled in two parts, one deterministic and one stochastic. The first, deterministic part of the drag is calculated assuming that the droplets are spherical. The calculation is then done using a spherical drag law with parameters taken for different Re number regions from Morsi and Alexander [22, 20].

The second, stochastic part of the drag, models the effect of random turbulent eddies applying their momentum to the droplet. This is modelled using a discrete random walk model (DRW) which adds a normally distributed random velocity fluctuation to the particle. The magnitude of the velocity fluctuation is calculated in equation 2.16 where ξ is a normally distributed random number. This velocity fluctuation u' is then applied to the particle for the estimated lifetime of a turbulent eddy, $2T_L$, which is calculated using equation 2.17. The value for C_L should be calibrated for the local flow situation. However, this was not done and a default C_L value of 0.15 was used [20].

$$u' = \xi \cdot \sqrt{\frac{2k}{3}} \tag{2.16}$$

$$T_L = C_L \frac{k}{\varepsilon} \tag{2.17}$$

2.5.2 Vaporisation

The liquid that is sprayed into the system is a mixture of sulfuric acid and water. Evaporation of a multicomponent mixture is modelled in two regimes, a non-boiling and a boiling one. In the non-boiling regime the mass transfer of species i is solved for by using equation 2.18. This equation considers the effect of a rapid evaporation on the rate of convective transfer, the Stefan flow, where B_{mi} is the mass Spalding number in equation 2.20. The mass transfer parameter k_{ci} is calculated using the Sherwood expression in equation 2.19 [20].

$$\frac{dm_i}{dt} = A_p k_{ci} \rho ln(1 + B_{mi}) \tag{2.18}$$

$$Sh = \frac{k_{ci} d_p}{D_{im}} = 2.0 + 0.6 Re_d^{1/2} Sc^{1/3} \tag{2.19}$$

$$B_{mi} = \frac{Y_{is} - Y_{i\infty}}{1 - Y_{is}} \tag{2.20}$$

The boiling regime is applied when the sum of the partial pressures of the species over the droplet is equal to the total pressure surrounding the particle, $P_{tot} = \sum P_i$. The mass transfer of species i is then calculated using equation 2.21 where the driving force is partly the net radiative heat transfer and the Spalding heat transfer number calculated in equation 2.22. For both regimes, the energy balance for the particles is solved according to equation 2.23 [20].

$$\frac{dm_i}{dt} = x_i \frac{\pi d_p \lambda}{c_p} (2 + 0.6 Re_d^{1/2} Pr^{1/3}) ln(1 + B_{Ti}) + \frac{x_i}{h_{vap,i}} A_p \epsilon_p \sigma (\Theta_R^4 - T_p^4) \tag{2.21}$$

$$B_{Ti} = \frac{c_p (T_\infty - T_p)}{h_{vap,i}} \tag{2.22}$$

$$m_p c_p \frac{dT}{dt} = A_p \epsilon_p \sigma (\Theta_R^4 - T_p^4) + h A_p (T_\infty - T_p) + \sum \frac{dm_i}{dt} (h_{vap,i}) \tag{2.23}$$

2.6 Turbulent mixing modelling

Chemical reactions occur when reactants coexist at a location but when the chemical reaction is faster than the species transport the overall reaction rate is not only controlled by the kinetic reaction rate. In the case of using a finite volume RANS model to describe the turbulence, the cells are larger than the turbulent structures. This means that if the chemistry is faster than the turbulent transport, the reactions take place not with bulk concentration in the cell but on a smaller non-resolved scale. A subgrid model for the description of the reactions and mixing is therefore needed. The first model used in this case is the eddy dissipation concept model. The other is the eddy dissipation model which is not to be confused with the aforementioned model.

2.6.1 The eddy dissipation concept model

In the EDC model, chemical reactions are assumed to occur in turbulent regions where there is a dissipation of turbulent kinetic energy. In these regions, the reactions occur in so called fine structures, which are in the size of the Kolmogorov length scale [23]. The dimensionless length scale of these fine structures are expressed as:

$$\xi^* = 2.1377 \left(\frac{\nu\varepsilon}{k^2}\right)^{0.25} \tag{2.24}$$

The length scale may be cubed, giving a certain volume fraction of a cell, ξ^{*3} where chemical reactions occur over a time scale τ^* [24]. In the standard EDC, the time scale is related to the mixing time scale for the Kolmogorov length scale and is given as [25]:

$$\tau^* = 0.4082 \left(\frac{\nu}{\varepsilon}\right)^{0.5} \tag{2.25}$$

The fine structures are solved in a perfectly stirred reactor (PSR) at steady state, where the reactions proceed at constant pressure. The kinetic reaction rate $\hat{R}_i$, for chemical species i reacting with N species based on the inlet concentrations C_j of species is [24, 25, 26]:

$$\hat{R}_i = \Gamma(\nu_i^{''} - \nu_i^{'}) \left(k_f \sum_{j=1}^{N} C_j^{\eta_j^{'}} - k_b \sum_{j=1}^{N} C_j^{\eta_j^{''}} \right) \tag{2.26}$$

The final apparent source term, R_i, for each chemical species i is then calculated using equation 2.27 where ρ is the bulk density, Y_i^* and Y_i are the respective mass fractions of species i in the fine structure and in the bulk. This apparent rate is then compared to the kinetic rate at Y_i and the smallest of these two is applied [20].

$$R_i = \frac{\rho}{\tau^*} \frac{(\xi^*)^2}{[1 - (\xi^*)^3]} (Y_i^* - Y_i) \tag{2.27}$$

2.6.2 ISAT

ISAT stands for In-Situ Adaptive Tabulation and is an algorithm to enhance the computational speed of stiff and detailed chemistry. In ISAT, the reaction space is tabulated rather than solved by direct integration (DI) [20]. This can reduce the computational time by three orders of magnitude [27].

Briefly explained, the reaction space is tabulated in the leaves of a binary tree, a data structure. In each leaf there is a record composed of, among others, a tabulated composition vector ϕ_0 and its Ellipsoid of Accuracy (EOA) which covers ϕ_0 [28]. The tabulated composition vector can be defined as [20]:

$$\phi_0 = (Y_1, Y_2, ..., Y_N, T, p) \tag{2.28}$$

Let ϕ_q be the queried composition vector. This composition vector may lie near a ϕ_0, whose EOA covers ϕ_q. If ϕ_q lies within an EOA of a ϕ_0, a linear interpolation according to equation 2.29 is retrieved. Otherwise, the reaction state is obtained by DI, as given by equation 2.30 [28].

$$R^l(\phi^q) = R(\phi^0) + \partial R \tag{2.29}$$

$$R(\phi_q) = \phi_q + \int_0^{\Delta t} S dt \tag{2.30}$$

After DI, a local error is calculated:

$$\varepsilon = \left| B(R(\phi^q) - R^l(\phi^q) \right| \tag{2.31}$$

If $\varepsilon < \varepsilon_{tol}$, ε_{tol} being a specified tolerance, the EOA of the leaf is grown to cover ϕ_q and $R(\phi^q)$ is returned. If $\varepsilon > \varepsilon_{tol}$, adding is performed. Thus, the leaf containing ϕ_0 is transformed into a node, with two outgrown leaves, containing the respective records of ϕ_0 and ϕ_q [28].

2.6.3 The eddy dissipation model

Another approach to modelling chemical reactions in turbulent flows is the eddy dissipation model, which is not to be confused with the eddy dissipation concept. In this model the reaction rate is evaluated as the smallest value of the kinetic rate and the respective mixing rates in equation 2.32 and 2.33. These two mixing expressions are controlled by the empirical parameters A and B, equal to 4 and 0.5 respectively. This model is less complex compared to the eddy dissipation concept model and is not suitable for multistep chemical reactions but works well with simple global reactions [20].

$$R_i = \nu_i' M_{w,i} A \rho \frac{\varepsilon}{k} min(\frac{Y_R}{\nu_R' M_{w,R}}) \tag{2.32}$$

$$R_i = \nu_i' \nu_i' M_{w,i} A B \rho \frac{\varepsilon}{k} \frac{\sum_P Y_P}{\sum \nu_j'' M_{w,j}} \tag{2.33}$$

3
Methodology

In the attempt to construct a computational model of the sulfation process in the Renova boiler several types of software and computational methods were used. The evaporation of the acid spray and the integration of the chemical reaction model was done in the 3D CFD software ANSYS Fluent 18.0. Validation of mechanisms, sanity checks and comparisons were done using simpler PSR and PFR models at steady state in ANSYS CHEMKIN 18.0.

3.1 Flow and turbulence modelling

An accurate solution requires an accurate prediction of the flow and turbulence which shall be coupled with the modelling of chemical reactions. One such solution for the turbulent flow in the Renova boiler was obtained by Sundborg and Tärnåsen [3], where the turbulent flow was solved in steady state with the Realizable $k - \varepsilon$ model. This is appropriate, as there is a swirl in the boiler, as shown in figure 3.1. In addition, the solution had been validated. Therefore the solution was used with the only addition of six inlets for the spray modelling.

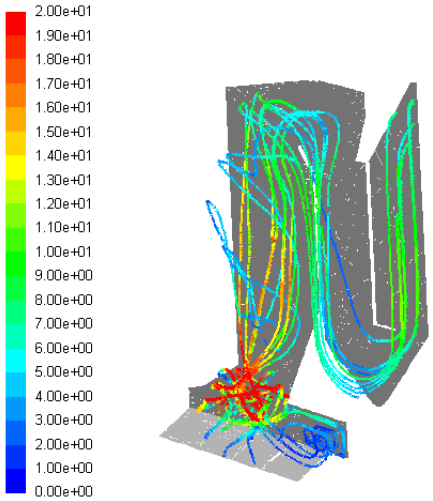

Figure 3.1: Pathlines coloured with velocity magnitude in the boiler. The vertical plane is the outermost wall whilst the horizontal plane is the primary air inlet.

3.1.1 Boundary conditions

In the previous thesis work, inlet mass flow into the fired grate was determined by mass balances based on plant data [3]. All walls were treated with no slip boundary conditions. For the treatment of the boundary layer near the wall, non-equilibrium wall functions were used. The motivation behind the selection of non-equilibrium wall functions was the swirling flow and flow impingement [29, 7]. The inlet velocity of the nozzles were calculated based on nozzle dimensions and flow rates.

3.2 Energy modelling

A complete, validated solution of the temperature field in boiler was produced by Sundborg and Tärnåsen [3]. This was done using a fixed gas inlet temperature of 1484 K based on a total energy balance and not by simulating the combustion. Furthermore, since the temperature is high and gas radiation contributes to a large share of the heat transfer, DO, along with a grey gas model by Johansson et al. [30] was used by Sundborg and Tärnåsen. These models were also used in this work.

3.2.1 Boundary conditions

The walls of the boiler are made of 5 mm thick steel tubes filled with water where the lower part has a 5 cm thick layer of concrete to shield it from the heat and corrosive elements. The water is saturated at 50 bar which has a boiling point of 537 K. The surface temperature of the walls was therefore set to this temperature. Due to the corrosive nature of the flue gas, the wall surfaces would be covered with a layer of deposits. The thickness of this fouling was not known and was used as a design parameter by Sundborg and Tärnåsen [3] in order to reach a desired outlet temperature.

The conductivity of the wall materials, steel, concrete and deposits used by Sundborg and Tärnåsen [3] were 45, 9 and 1 W/mK respectively. These were summed as following, based on the width of each material [3]:

$$\lambda_{wall} = \frac{L_{wall}}{\Sigma \frac{L_i}{\lambda_i}} \tag{3.1}$$

The internal emissivity of the walls was set to 0.79 based on oxidized steel at 600 °C while the emissivity of the burning waste at the bottom was set to an emissivity of 0. Measurements of the emissivity of waste was available but when used by Sundborg and Tärnåsen [3] a less realistic temperature result was obtained and instead, an emissivity of 0 was used. The addition of the sulfuric acid spray to

the system meant that additional temperature boundary conditions were needed, as the spray is significantly cooler than the flue gas. As such it has an impact on the temperature both locally and globally in the boiler. It was assumed that the liquid acid spray shared a temperature with the pressurized air and that the heat capacity of the extra flue gas is low enough that the entire flow has a temperature of 50 °C.

3.2.2 Discrete Ordinates

In terms of radiation modelling, the ordinates had 5 θ and 5 ϕ discretizations, $N_\theta = N_\phi = 5$. Along these two angles there was also a 3x3 pixellation. In general, when the energy equation was solved, 10 flow iterations were done between every evaluation of the DO. Depending on the distance from convergence either more or fewer flow iterations were done between each DO evaluation.

3.3 Spray modelling

The amount of sulfuric acid injected into the system was calculated based on known SO_2 dosage from the previous master thesis work [3]. This amounted to a flow rate of 0.0479 kg/s per nozzle, yielding a total of 0.2874 kg/s for all six nozzles. The sulfuric acid solution was composed of 15 wt% sulfuric acid and 85 wt% water.

3.3.1 Size distribution

The size distribution of the droplets from the nozzles were given by the nozzle manufacturer. The distribution was obtained using a Malvern 2600C laser diffraction particle sizer. The liquid used in the test was water at room temperature, which has a surface tension of 7.28 N/m, viscosity of 0.001 Pas and density of 1000 kg/m^3 [31]. Sulfuric acid at 50 °C has a similar viscosity, density and surface tension with air as water at 25 °C [32, 33, 34]. It was therefore deemed that the size distribution measurements would be similar enough to 50 °C sulfuric acid to be used directly.

It was also assumed that the measurements were done at a distance far enough away from the nozzle for primary breakup to be completed. Secondary droplet breakup was also neglected, as this was motivated with We = 0.05-1 and Oh = 0.01-0.15 in the simulation. Based on measurements [35] this would place the droplets in a region with little to no secondary breakup. In reality, there would be a minor secondary breakup. However, it was assumed that the final effect on the results would most likely be negligible.

The implementation of the size distribution was done with a curve fit to a Rosin-Rammler distribution. In Fluent, this distribution is implemented as:

$$Y_d = exp(-d/\bar{d})^n \tag{3.2}$$

where Y_d is the mass fraction of droplets with a diameter greater than d [36]. The distribution with the fitted parameters of $\bar{d}$ and n is shown in figure 3.2.

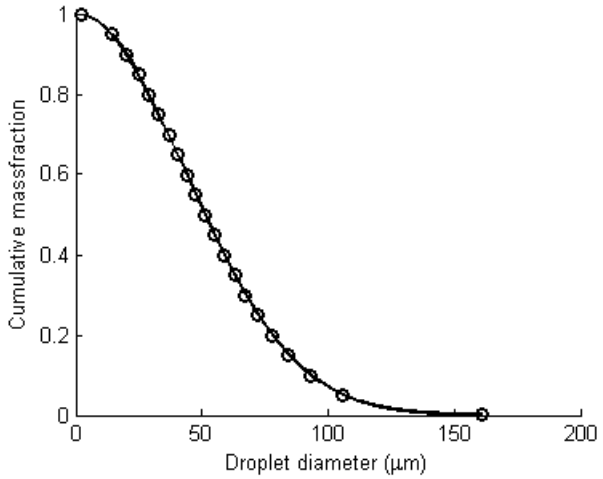

Figure 3.2: The fitted Rosin-Rammler distribution against the measured points, $\bar{d} = 61.5\ \mu m$, $n = 2.0034$.

3.3.2 Vaporisation

The liquid droplets injected into the system is a highly non-ideal system where H_2SO_4 rapidly decomposes into SO_3 and H_2O as expressed below:

$$H_2SO_4(l) \rightarrow H_2SO_4(g) \rightarrow SO_3(g) + H_2O(g) \tag{3.3}$$

Based on experiments on the evaporation of H_2SO_4, the initial decompositon step is very rapid at high temperatures. Studies have shown that above 450 °C H_2SO_4 completely dissociates into SO_3 and H_2O [37, 34]. The vaporisation process was therefore simplified into two steps, as listed in the reactions of 3.4-3.5.

$$H_2O(l) \rightarrow H_2O(g) \tag{3.4}$$
$$H_2SO_4(l) \rightarrow H_2O(g) + SO_3(g) \tag{3.5}$$

Applying equations 2.18 and 2.21 from section 2.5.2 requires that the droplet surface concentrations of H_2O and SO_3 are known. An equilibrium condition at the surface is assumed, meaning the the partial pressures of SO_3 and H_2O are equal to the saturation pressures of respective component. Data [38] for the partial pressures of H_2O, SO_3 and H_2SO_4 was available ranging from 10 wt% to 90 wt% sulfuric acid and 0 °C to 350 °C. The partial pressures of SO_3 and H_2SO_4 were added together in accordance with the assumption of complete and immediate dissociation into SO_3.

These were then fitted to polynomial curves to produce a continuous function with respect to temperature and acid fraction, as shown in figure 3.3.

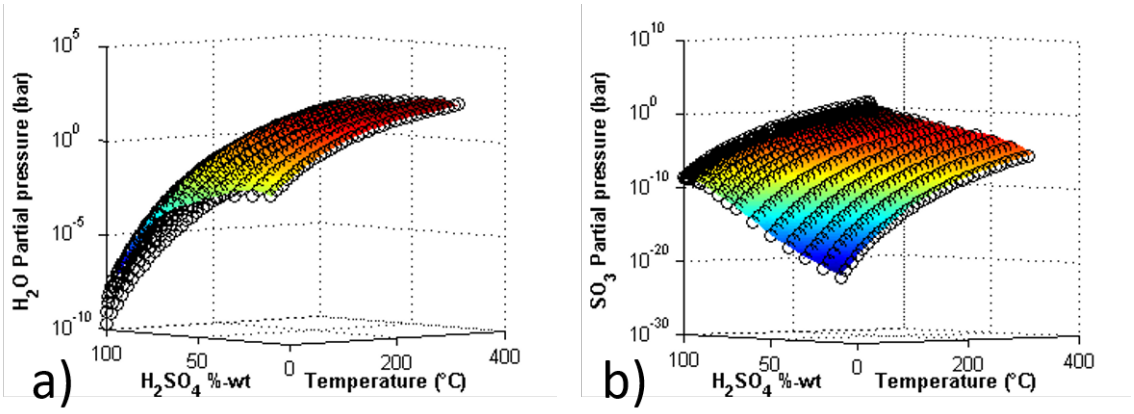

Figure 3.3: a) Surface plot of the H_2O vapour pressure polynomial as a function of temperature and mass percent of sulfuric acid. b) Surface plot of the SO_3 vapour pressure polynomial as a function of temperature and mass percent of sulfuric acid. The black circles represent data points.

This data was implemented into Fluent using a UDF that returned the value from the polynomials based on the temperature and composition of the evaluated droplet. The fitted polynomials are found in Appendix A.1. Statistical R^2 values for the three polynomials are shown in table 3.1 which shows a good fit of the data. However, two parameters in the SO_3 polynomial are not significant with 95 % bounds, one parameter in the H_2SO_4 polynomial is not significant in 95 % bounds and one parameter is not significant in the H_2O polynomial. This makes the polynomials slightly over-parameterized but is not of practical importance for the evaluation of the vapour pressure. Also, from these polynomials the boiling point of the liquid can be derived and is shown in figure 3.4.

Polynomial	R^2
H_2O	0.9840
SO_3	0.9979
H_2SO_4	0.9999

Table 3.1: Table of R square values for the fitted polynomials.

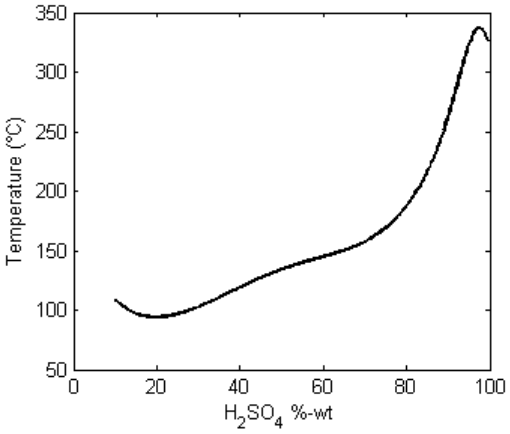

Figure 3.4: A graph of sulfuric acid boiling temperature at atmospheric pressure based on the fitted polynomials.

3.3.3 Inlet conditions

The sulfuric acid spray has a temperature of 50 °C and is boosted by an auxiliary stream of flue gas extracted from a latter part of the boiler. The amount of auxiliary flue gas was calculated based on the knowledge of the geometry of the tube: known inner diameter, outer diameter and wall thickness along with an estimated average velocity of 60 m/s using the ideal gas law. Further, the amount of atomizing pressurized air added to the spray was calculated based on manufacturer specifications and scaled on the amount of liquid spray. This gave the individual mass- and volume flow rates of the sulfuric acid, pressurized air and flue gas. With known flow rates and a known injection diameter, a droplet injection velocity of 45 m/s was determined.

It was assumed that all entering spray droplets shared the same velocity magnitude and temperature. The spray was a circular cone with a width of 7° perpendicular to the wall. This circular cone was modelled by adding an additional random velocity between 0 and 5.5 m/s in the x and y direction to the entering droplets. The addition was not done as to preserve the velocity magnitude as a few droplets had a velocity greater than 45 m/s. The velocity could therefore be up to 45.66 m/s which was accepted as negligible.

3.3.4 Particle tracking

Using 45 m/s as an initial velocity and an approximated cell length of 0.05 m the expected cell residence time would be 1.1 ms. For an adequate resolution of the droplet trajectory a time step of approximately half the cell residence time, 0.5 ms, was chosen. Further, with the d^2 law a droplet lifetime of 0.1 s was estimated which would mean that the vaporisation process was resolved in approximately 200 steps. The trajectory was integrated with a trapezoidal scheme with a tolerance of 1e-5.

No types of collisions or droplet coalescence was taken into account in the simulation. Such models are computationally expensive and since the droplets all travel in the same general direction, droplet collision and coalescence was neglected. Wall collisions were also neglected, as the droplets were injected perpendicularly from the wall. Additionally, the estimated life time of 0.1 s makes it highly improbable that any droplet would reach the opposite wall.

Based on the size distribution and having spherical droplets the estimated number of droplets entering the system is 1.2e10 per second which is unfeasible to simulate both computationally and memory wise. Therefore, the particles were tracked as parcels which were sized using the standard method in ANSYS Fluent as defined below [36]:

$$NP = \dot{m}\frac{\Delta t}{m_p} \tag{3.6}$$

NP is the number of particles in the released parcel, $\dot{m}$ is the mass flow rate, Δt is the time step and m_p is the particle mass.

3.3.5 Chemistry decoupling and domain reduction

Performing a transient simulation of the spray simultaneously with the chemistry solver is not computationally feasible; therefore droplet simulations were solved separately. Decoupling of the vaporisation and the chemistry is primarily motivated by the chemistry not changing the bulk composition of the gas with respect to H_2O nor the bulk temperature. The chemical reactions do however reduce the amount of SO_3 in the system which could have an impact on the evaporation part of the mass transfer. This effect should be negligible however as the gradient of SO_3 was similar in two cases when both the reaction chemistry and the evaporation was enabled and when only vaporisation was enabled.

The decoupled solution for the spray was simulated in a separate, smaller domain with a lower resolution since there is no need to resolve large species gradients that can affect the chemistry. Since it was simulated in a different mesh the solution had to be interpolated into the mesh where the chemistry was solved. This interpolation was done for the SO_3 and H_2O species and did not include the 790 kJ/s of energy from heating and vaporization of droplets. This amount of neglected energy would be equivalent to a temperature decrease of 14 K for the flue gas. The amount of neglected energy was deemed acceptable since 14 K is not enough to have a considerable impact on the results. A representation of the smaller domain is shown in figure 3.5. This corresponds to the part of the boiler before the first bend, which allowed a greatly reduced number of cells to be used.

In the same figure an overview of the droplet distribution can be seen with the parcels coloured by liquid phase temperature. The length which the droplets penetrate into the domain is very short; the average residence time of the droplets

was only 0.05 seconds. This is reasonable since the d^2 law gave 0.1 seconds. The maximum residence was approximately 0.21 seconds. In addition, a $St << 1$ was determined based on the lifetime of a turbulent eddy, which is in accordance with the observed behaviour of the droplets in the figure.

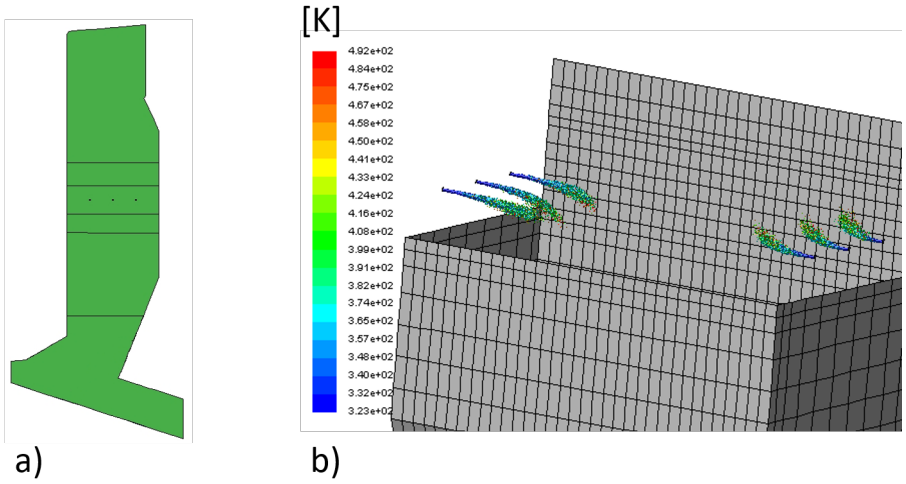

Figure 3.5: a) The reduced domain used for spray simulations . b) Droplet parcels coloured by liquid phase temperature, sized by parcel diameter and scaled up 50 times.

3.4 Species modelling

Modelling the sulfation process requires solving for the various species of interest in the system by applying the kinetic model outlined in section 2.2.1. This means solving the reaction rate equations and the transport equations for all these species in parallel. The degree of sulfation was evaluated by comparing the outlet molar flow rate of potassium bounded to sulfur with the inlet molar flow rate of potassium. This included the species K_2SO_4 and $KHSO_4$ which were the most common potassium species present at the outlet.

3.4.1 Boundary conditions

The combustion occurring in and directly above the firing grate was not simulated as this was outside the scope of this work. Instead, the transport of SO_3 together with the acid spray was solved without reaction which gave how far the injected SO_3 reached in the direction of the firing grate. Using an average molar fraction of 10 ppm SO_3 as a cutoff, the height of 6 m above the firing grate was chosen as the boundary height for the chemistry. Below this height no reaction integration is performed; only flow and species transport is solved. This cutoff line can be seen in figure 2.4, section 2.3, where it is located directly above the grate. The reason for the high SO_3 concentrations below the spray inlet is due to the rotating flow in

that part of the boiler which transports the SO_3 downwards. The rotating flow can be observed in figure 3.1.

Since no chemistry was solved below the cutoff plane it was assumed that the gas entering the system below this point was perfectly mixed. With this assumption the PFR model produced by Sundborg and Tärnåsen [3] was used to extract a gas composition at the cutoff plane. However, in this model CO and O_2 was continuously injected along the length of the boiler. This means that extracting a composition before these injections were fully realised would result in a loss of total mass. Therefore the rate of injection of these substances was increased, ensuring that all mass is injected before the extraction height. This would likely mean that the degree of sulfation is slightly overestimated since there would be slightly more radicals present. The resulting composition is given in table 3.2.

Table 3.2: Inlet composition extracted from the work of Sundborg and Tärnåsen [3]. $K_2SO_4(B)$ is the condensed form of K_2SO_4.

Species	ppm	Species	ppm
SO_2	50	CO	3.3
SO_3	1.9	CO_2	102 000
K	1.9e-4	H	6.5e-3
KO	3.9e-5	O	0.14
KOH	0.72	OH	20
KCl	227	H_2	0.9
K_2Cl_2	0.68	O_2	51 500
$KHSO_3$	1.6e-6	HO_2	0.015
KSO_4	2.8e-4	H_2O	177 000
KSO_2	1.2e-5	$HOSO_2$	4.4e-6
KSO_3	1.7e-4	HCl	549
$KHSO_4$	0.18	Cl	3.35
KSO_3Cl	1.0e-3	$K_2SO_4(B)$	92.5
K_2SO_4	5.1e-3	N_2	668 000

The gas composition at the spray inlets was based on the recirculating flue gas. Since no specific composition was available for this stream, the bulk species of H_2O, CO_2, O_2 and N_2 with the same composition as that of the inlets at the bottom of the boiler was used.

3.4.2 Reaction mechanism reduction

The size of the complete reaction mechanism proposed by Hindiyarti et al. is prohibitive to run in a CFD simulation; 72 species requires 71 transport equations to be solved. These are also coupled with 288 reactions, some of which result in stiff equations, difficult to integrate. Therefore a reduced form of the reaction mechanism had to be created.

In order to create a reduced mechanism a reaction space for the sulfation had to be established. This means selecting parameters that are important for the sulfation process and varying them in the range present in the system. The concentration range of the main species (SO_3, SO_2 and KCl) in the sulfation process were established using different methods. The concentration range for SO_3 was based on the droplet vaporisation simulation with chemistry decoupling as described in section 3.3.5, where the concentration range was 1-1000 ppm. The SO_2 and KCl concentrations were based on an expected 70 % degree of sulfation, resulting in the respective ranges of 50-200 ppm and 1-200 ppm. In addition, the temperature range was 600-1500 K and the reaction timescale 5-15 milliseconds. These were obtained from the CFD simulations, where the temperature range was based on the temperature profile of the boiler and the reaction timescale was based on cell size, flow velocity and fine scale eddy lifetime.

A steady state PSR CHEMKIN model was then based on these conditions where all aforementioned variables were discretized into three points resulting in 243 PSR solutions per evaluation. The DRGEP reduction algorithm was applied to this system with an increasing level of error tolerance with regards to SO_3, SO_2 and KCl until a reasonably sized mechanism was acquired. The average error of the mechanism was 1.5 % and the maximum error was 2 %. This reduced mechanism had 27 species and 89 reactions but was missing the condensation reaction of K_2SO_4 which is known to be important since it is the final step in the sulfation process. The reason it was removed by the DRGEP algorithm is most likely due to the small residence time used in the reduction. It was therefore added to the mechanism, giving in total 28 species with 90 reactions.

An overview of the magnitude of the releative error can be seen in the figures of 3.6-3.8 below. Most notably it can be observed that the relative error for the SO_2 reaction rate is far greater than the reaction rates of SO_3 and KCl, reaching an approximately 2 %. This means that any CFD simulation using this mechanism has a minimum uncertainty of 2 %.

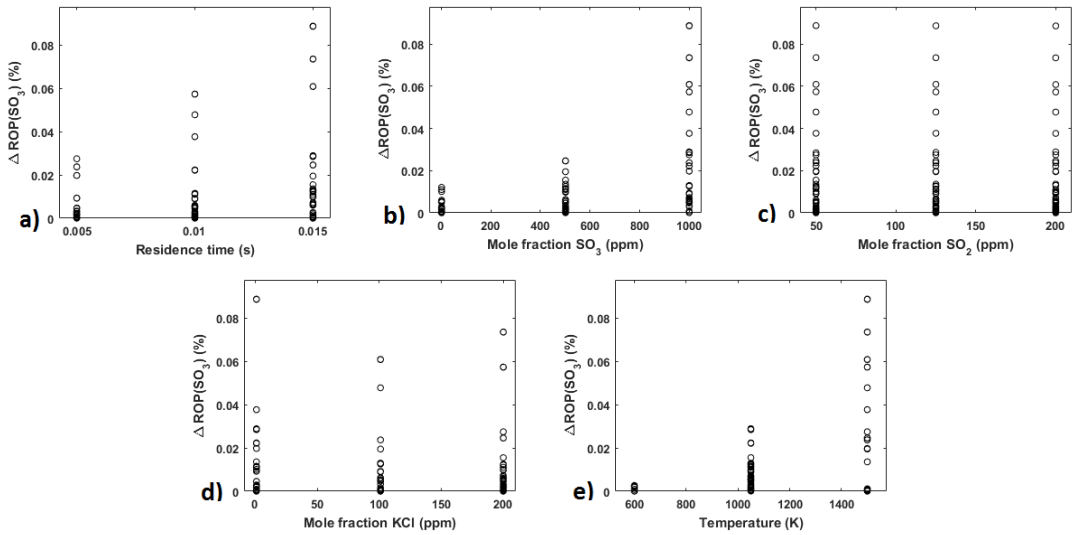

Figure 3.6: Plots of relative SO_3 reaction rate error with regards to the different variables in the reaction space. a) Residence time. b-d) Respective molar fraction of SO_3, SO_2 and KCl. e) Temperature.

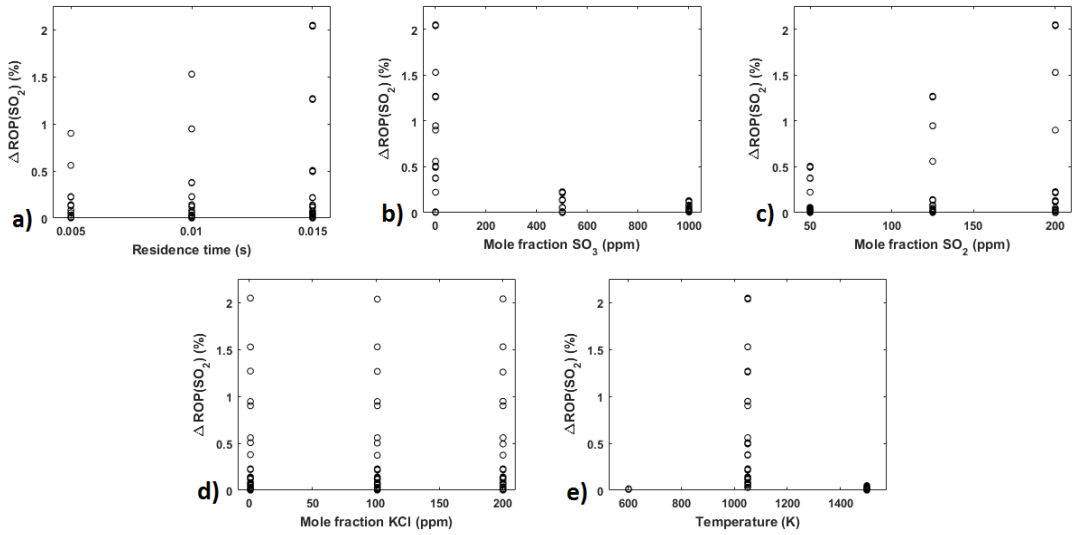

Figure 3.7: Plots of relative SO_2 reaction rate error with regards to the different variables in the reaction space. a) Residence time. b-d) Respective molar fraction of SO_3, SO_2 and KCl. e) Temperature.

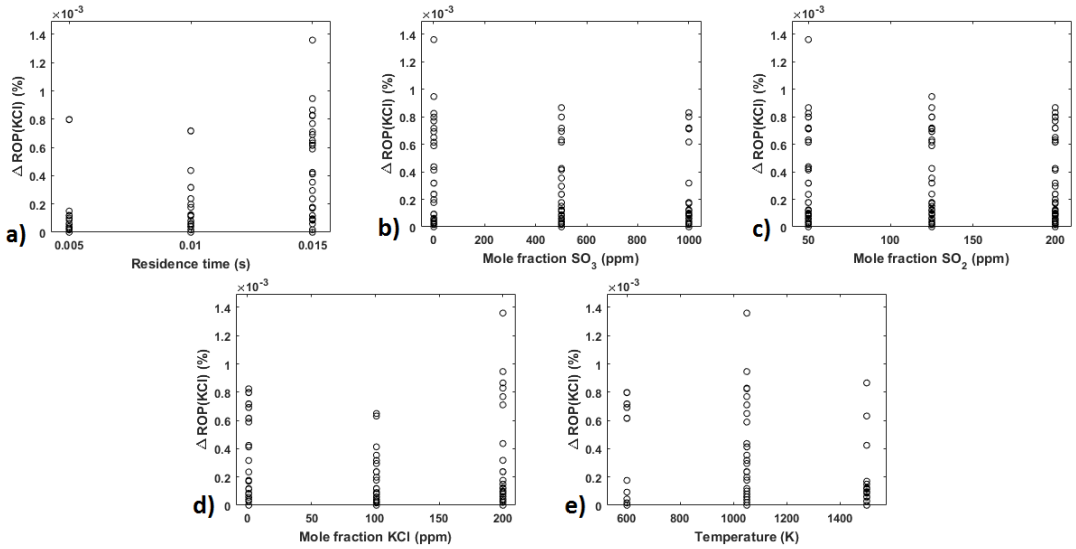

Figure 3.8: Plots of relative KCl reaction rate error with regards to the different variables in the reaction space. a) Residence time. b-d) Respective molar fraction of SO_3, SO_2 and KCl. e) Temperature.

In order to determine if any reactions with timescales much larger than 15 milliseconds were excluded in the reduced mechanism, the reduced mechanism and full mechanism were compared using the PFR model produced by Sundborg and Tärnåsen [3]. The residence time in the PFR model was 7.53 seconds which means that if any important reactions with timescales in that order or smaller were excluded, there would be significant errors in the PFR comparison. The results of the comparison can be seen in figure 3.9 where there are no significant errors. The max error point and the endpoint error point for respective concentration profile of SO_3, SO_2 and KCl were as follows: 1.99 ppm, 1e-6 ppm; 3.15 ppm, 1.27 ppm; 5.17 ppm, 0.33 ppm. In total these errors were accepted as small enough to be negligible.

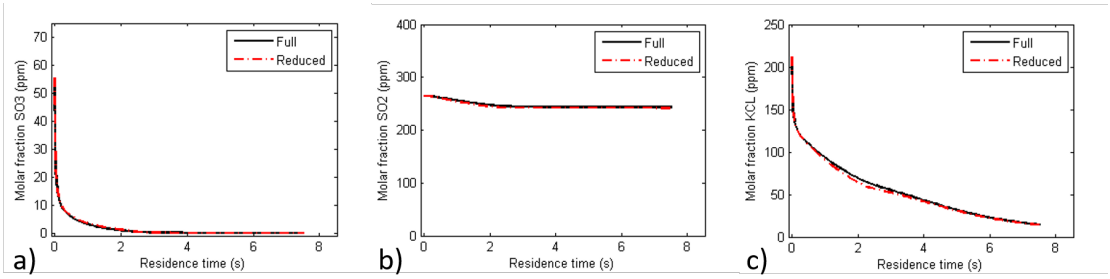

Figure 3.9: Results of running the full and reduced mechanisms in the PFR model produced by Sundborg and Tärnåsen [3]. a-c) The respective molar fractions of SO_3, SO_2 and KCl versus residence time.

3.4.3 Species diffusivities

There is a large number of species involved in the model and for many of these there is little to no data on transport properties available; therefore an approximation was used. The approximation was based on that the effective diffusivity of a species is calculated as the sum of laminar diffusivity and turbulent diffusivity, see equation 3.7. Therefore as long as the turbulent contribution to the sum is several orders of magnitude larger than the laminar part, an accurate laminar diffusivity is not needed.

$$\vec{J_i} = -(\rho D_{im} + \frac{\mu_t}{Sc_t})\nabla Y_i \tag{3.7}$$

Using Lennard-Jones constants for bulk species such as O_2 and CO_2, the estimated order of magnitude of the laminar diffusivity was 1e−4 m^2/s. The average turbulent viscosity in the system however was 0.41 m^2/s which, using a turbulent Schmidt number of 0.7, would make the turbulent contribution to the diffusion approximately 6000 times greater. Therefore a universal, constant value for the laminar diffusivity of all species was set to 1e−4 m^2/s.

3.5 Numerics

3.5.1 Mesh

A mesh consisting of approximately 450 000 tetrahedral cells was used as a base case for the simulations. The mesh used for the base case simulation is shown in figure 3.10. In terms of mesh quality, the average aspect ratio and skewness was 2.4 and 0.28. The maximum skewness was 0.93. This is in accordance with best practice guidelines [29].

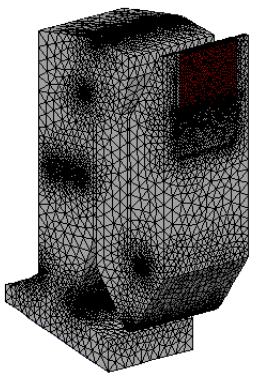

Figure 3.10: The 450 000 cell mesh used as the base case in the simulations.

3.5.2 $y+$

In figure 3.11, a contour plot of the $y+$ values for one of the more refined meshes is shown. It can be observed that a considerable amount of cells do not fulfil the $y+$ criteria of $30 < y+ < 100$. However Re in the boiler is approximately 3e5 and based on the law of the wall $y+$ is in range of 1e3. Therefore the $y+$ should be acceptable.

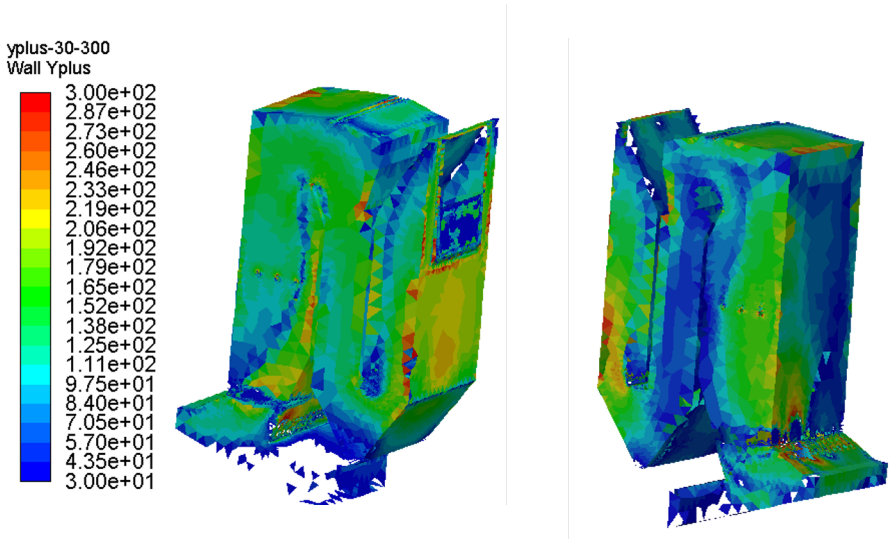

Figure 3.11: $y+$ contour plot of one of the more refined meshes.

Also, there are holes in the contour where $y+ < 30$. However, these are stagnant zones and lower $y+$ values can be accepted. The solution can be regarded as fair with respect to $y+$ and an additional refinement of $y+$ would most likely not impact the results significantly.

3.5.3 Convergence

Convergence in the simulations was evaluated by calculating global mass and energy balances as well as individual molar balances for respective element (K, S, O, H, Cl, C, N). A difference less than 5 % was deemed sufficient. For all global balances, the imbalance in % was defined as:

$$\dot{X}_{diff} = \frac{\dot{X_{in}} - \dot{X_{out}}}{\dot{X_{in}}} \cdot 100 \tag{3.8}$$

where $\dot{X}$ is either the flow rate of mass, energy or atomic elements in or out from the system.

4

Results and Discussion

The results from the various CFD simulations are presented in this section. There is a complete overview of the outlet molar fractions, DoS, SO_3/SO_2 mass ratio, individual molar imbalances and total mass- and energy imbalances in table A.1.

4.1 Initial results

In the initial simulation, where the reduced chemical mechanism was implemented along with the EDC model, the DoS was overestimated and the SO_3 to SO_2 conversion was underestimated. This is observed in table A.1 under the column for the base case, where the SO_3/SO_2 mass ratio is much higher than measured. Further, the DoS is greater than 100 %. This is due to the definition of DoS where the outlet molar flow rate of potassium sulfates is compared to the inlet molar flow rate of potassium. Due to the molar imbalance of potassium the outlet flow rate of sulfated potassium can be greater than the inlet flow rate of potassium. Figure 4.1 is a contour plot displaying the resulting levels of SO_3 found in the system.

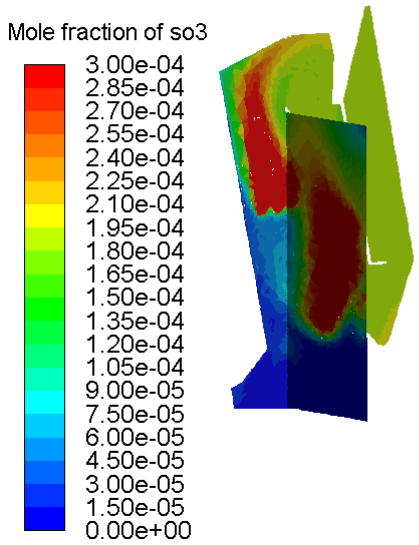

Figure 4.1: Contour plot of SO_3, 0-300 ppm. The leftmost plane is 1 m from the left wall. The second plane is a mid cross section of the boiler.

4.1.1 CO injection in CHEMKIN

As described in the previous section, the initial simulation gave an overestimated DoS and an underestimated SO_3 conversion. A possible solution was based on the previous work of Sundborg and Tärnåsen [3]. In their work, a continuous injection of CO was used to generate radicals in order to increase the overall reaction rate. A similar solution to the SO_3 conversion was therefore investigated.

The PFR model was modified by changing the inlet composition of the injected sulfur. In the previous work of Sundborg and Tärnåsen [3], a 80/20 SO_3/SO_2 molar mix was used. However, as the conversion of SO_3 to SO_2 was the interesting parameter, only SO_3 was injected. In figure 4.2, it can be observed that the presence of CO greatly affected the conversion of SO_3.

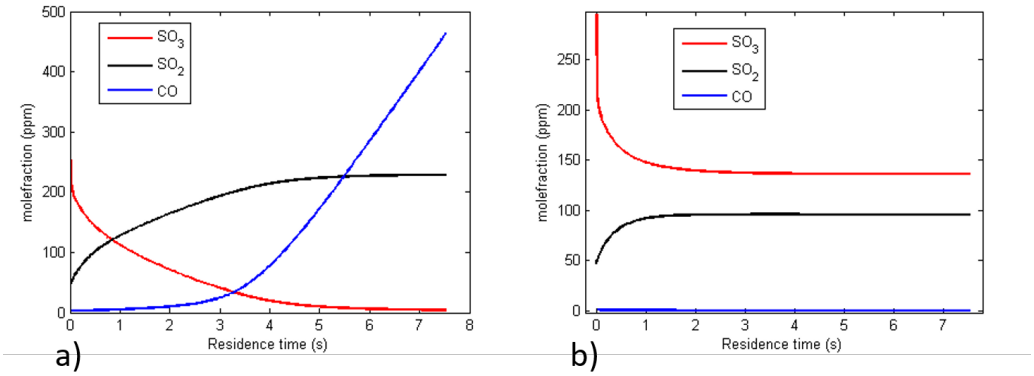

Figure 4.2: Mole fraction of SO_3, SO_2 and CO versus residence time in the PFR. a) With CO injection. b) No CO injection.

4.2 CO injection in Fluent

Based on the CHEMKIN results observed in figure 4.2 different amounts of CO was injected into the boiler in the CFD simulations. The CO was injected heterogeneously by changing the inlet composition in the marked area of the fired grate as shown in figure 4.3. The marked area corresponds to the area where a large amount of combustible gases are released during the combustion. In addition, by selecting this area, the mixing limitation of CO was also taken into account.

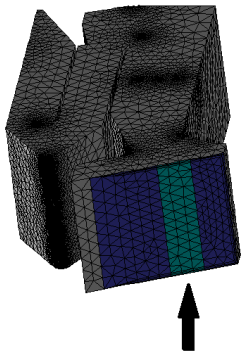

Figure 4.3: Location of the CO injection coloured in cyan.

4.2.1 Sulfation with 200 ppm CO

An increase of 200 ppm CO in the marked area gave a minor increase in the conversion of SO_3 to SO_2, as shown in table A.1. As the outlet concentration of SO_3 changed by only a few ppm, the amount of radicals added was clearly insufficient.

4.2.2 Sulfation with 25 000 ppm CO and 75 000 ppm CO

Based on the results in the previous section, two respective cases with 25- and 75 000 ppm injected CO were simulated. The choice of 25- and 75 000 ppm CO was under the assumption that part of the combustion process occurs higher in the reactor. The CO_2 in the initial composition of the marked area in figure 4.3 was thereby converted to CO and O_2. As observed in table A.1 and figure 4.4, the conversion of SO_3 was still underpredicted but increased noticeably compared to the base simulation.

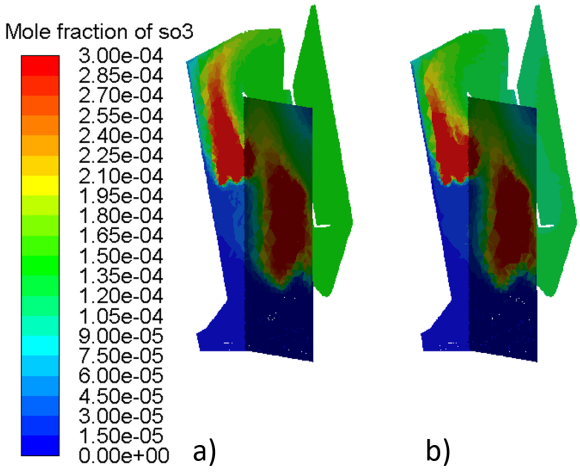

Figure 4.4: Contour plots of SO_3, 0-300 ppm. a) 25 000 ppm CO injection. b) 75 000 ppm CO injection. The leftmost plane is 1 m from the left wall. The second plane is a mid cross section of the boiler.

4.2.3 Sulfation with 321 000 ppm CO and CO and H_2

Based on the results of the 25- and 75 000 ppm CO injection cases 80 mol% of all carbon at the primary and secondary air inlets was converted into CO. This represents 40 % of the combustion occuring above the inert region. The resulting CO molar fraction at the injection area was therefore 321 000 ppm. As observed in table A.1 the results of this simulation only differed marginally from the 25- and 75 000 ppm CO injection cases with respect to SO_3 conversion. This indicates that it is not possible to inject a realistic amount of CO into the system that would not underpredict the SO_3 conversion.

An additional case was simulated based on the known C/H mass ratio in the waste fuel. All CO_2 at the primary and secondary air inlets was converted to CO. Based on the mass ratio, H_2O was converted to H_2 and O_2. This resulted in molar fractions of 308 000 ppm CO and 247 000 ppm H_2 in the marked area in figure 4.3. As observed in table A.1 and figure 4.5 the results of this simulation only differed marginally from the injection of 321 000 ppm of CO.

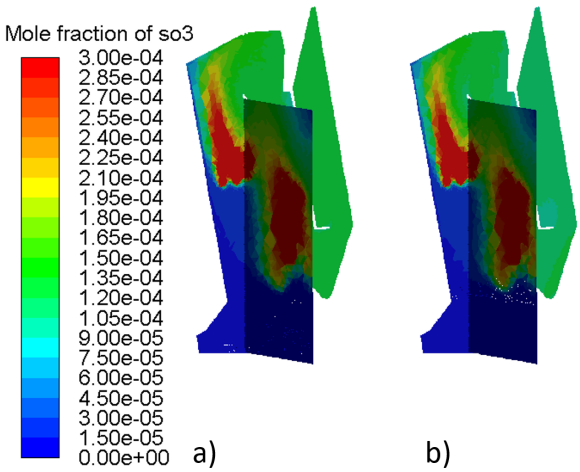

Figure 4.5: Contour plots of SO_3, 0-300 ppm. a) 321 000 ppm CO injection. b) CO and H_2 injection. The leftmost plane is 1 m from the left wall. The second plane is a mid cross section of the boiler.

4.2.4 Global mechanism with eddy dissipation

A global mechanism based on an assumption that the added CO in the PFR model in section 4.1.1 represents a realistic amount of radicals was developed. This was implemented in the CFD model together with the eddy disspation model.

4.2.4.1 Development of global mechanism

The global mechanism consisted of the three apparent reactions of 4.1-4.3.

$$SO_3 \rightarrow SO_2 + 1/2O_2 \tag{4.1}$$
$$SO_2 + 1/2O_2 \rightarrow SO_3 \tag{4.2}$$
$$H_2O + SO_3 + 2KCl \rightarrow K_2SO_4 + 2HCl \tag{4.3}$$

The data used for these kinetics was the PFR model with CO injection described in section 4.1.1 and removing all potassium from the system. This was to ensure that the reaction rates for SO_3 and SO_2 do not include sulfation. The adapted rate expressions for reactions 4.1-4.2 are shown in figure 4.6 and the corresponding Arrhenius parameters for the reactions are given in table 4.1. The reaction orders for SO_2 and SO_3 are 1 while the reaction order for O_2 is zero due to a constant O_2 concentration in the system. Reaction 4.3 was implemented by using the maximum allowed rate constant of 1e38 in order to ensure that the rate of sulfation is limited by mixing.

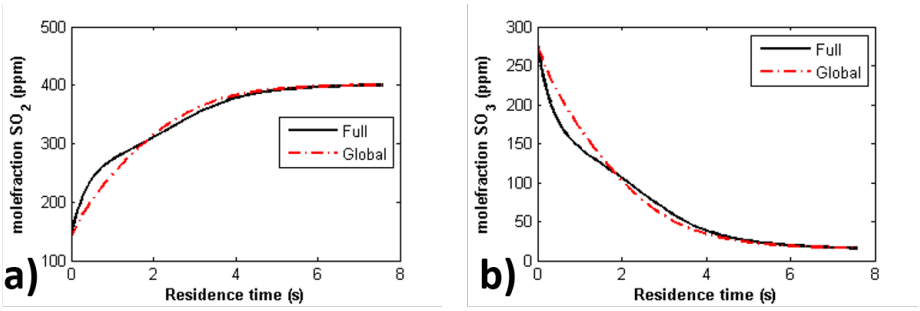

Figure 4.6: Comparison between the global and full chemical mechanisms for respective sulfur oxide. a) SO_2, b) SO_3.

Table 4.1: Rate fitted constants for the conversion of SO_3 to SO_2.

Reaction	A	β	E_a (J/Kmole)
4.1	6341	-1.173	10001
4.2	8738	-1.785	6060

4.2.4.2 CFD implementation

All three reactions were implemented together with the eddy dissipation model using the standard A value of 4 and B value of 0.5 for the two SO_3 to SO_2 reactions. This resulted in a higher SO_3 conversion closer to that of the measured plant data but the sulfation rate was too high; therefore different values for the mixing rate, A and B, for reaction 4.3 were tested. The results most consistent with measurements were a value of 0.5 for A and 4 for B. The results can be observed in A.1 and in figure 4.7.

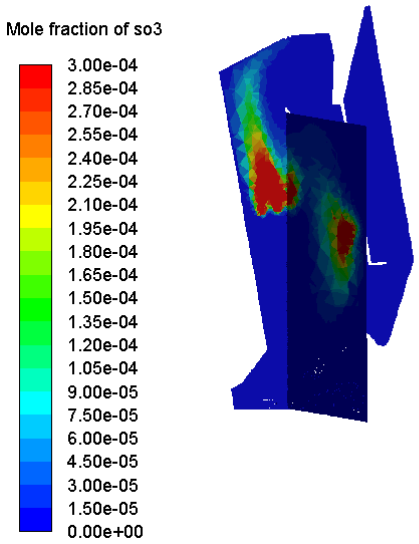

Figure 4.7: Contour plot of SO_3, 0-300 ppm. CFD simulation with the global mechanism and eddy dissipation. The leftmost plane is 1 m from the left wall. The second plane is a mid cross section of the boiler.

4.2.4.3 Model assessment

This global mechanism has a disadvantage as it is only fitted to the results of a single set of PFR data. This means that it is only representative for a small part of the reaction space that could potentially be found in the boiler. Further, it can be observed in figure 4.6 that there are noticeable discrepancies between the global and the full mechanism.

The accuracy of the sulfation process becomes questionable when the reaction rate is entirely controlled by mixing. One major issue is that there are no thermodynamic limitations to the sulfation reaction or the SO_3-SO_2 reactions, which in reality could affect reaction rates greatly. Also, in regions with low concentrations of KCl and SO_3, particularly in low temperature regions near the outlet, the rate of reaction 4.3 is most likely overestimated. This is because the finite rate would probably be limiting in this region. The overestimation of DoS observed in table A.1 for this case is probably due to this reason.

4.3 CHEMKIN sensitivity analysis

A sensitivity analysis was done in CHEMKIN to determine if uncertainties in the composition or temperature could be the reason behind the low SO_3 conversion. Therefore, the effect of chemical species that can generate radicals was investigated, along with a change in the boiler temperature. This was done as an alternative to the CFD simulations since 1D CHEMKIN simulations are easier and quicker to perform.

4.3.1 Species

Water vapour, oxygen and hydrochloric acid are all species that can generate radicals at high temperatures. Therefore, the inlet molar fractions of these species were varied as shown in figure 4.8. The results showed that none of them could have a significant impact on the SO_3 to SO_2 conversion.

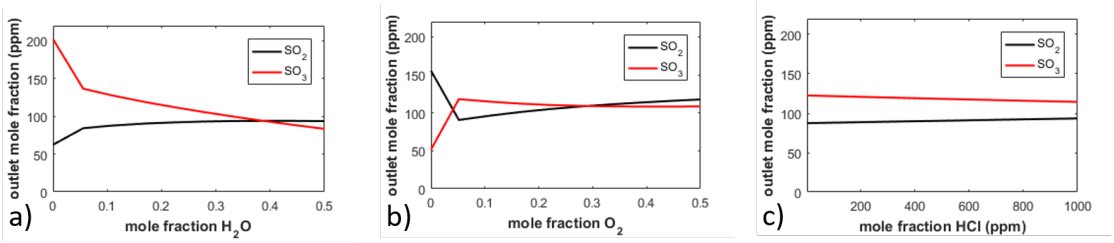

Figure 4.8: Outlet concentrations of SO_2 and SO_3 versus different inlet concentrations of radical generating species in the PFR. a) H_2O, b) O_2, c) HCl.

4.3.2 Temperature

Another important parameter is the temperature in the boiler. The validated temperature profile in the boiler is a temperature profile at steady state. However, in waste combustion, the moisture content in the waste may vary and cause variations in temperature. To analyse what effects the temperature profile could have on the SO_3 conversion an overall increase and decrease of 200 K was applied to the whole PFR temperature profile. The result is shown in figure 4.9 where an increase of about 100 K yields realistic outlet fractions of SO_3 and SO_2.

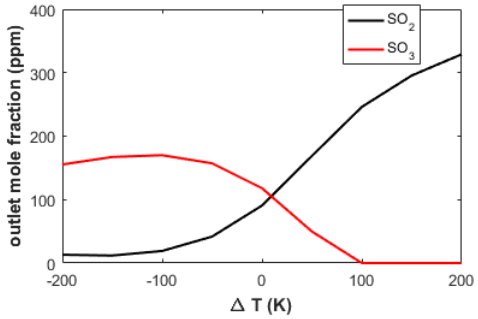

Figure 4.9: Outlet composition of SO_2 and SO_3 as function of a decrease or increase in the temperature profile.

4.4 CFD model evaluation

Based on the results obtained for all simulations in the previous section, it can be concluded that the model is not consistent with the experimental results. Both in the CFD and CHEMKIN simulations, it was shown that a low concentration of CO

lead to unrealistically high outlet concentrations of SO_3. This is an indication that the problem may lie in the chemical model rather than in the CFD model. However, errors in the CFD model must also be discussed and estimated.

4.4.1 Flue gas composition

An important aspect of the model is the lack of combustion modelling. Instead, a flue gas composition from the CHEMKIN case provided by Sundborg and Tärnåsen [3] was used for all inlets. The composition was obtained from a PFR, where CO and O_2 were continuously injected along the boiler height to provide a realistic amount of radicals. In addition, the full mechanism used in the CHEMKIN simulations does not contain a detailed combustion model but does contain the oxidation of CO and H_2. Thus, the fuel, oxidizer and air was represented by a mix of CO, O_2, H_2, H_2S, HCl, KCl and N_2.

The combustion is therefore not modelled in detail which could compromise the reliability of the flue gas composition. However, in the comparison of the outlet composition from the PFR to a representative composition, table 2.1.1, the values are in the right region. This together with the sensitivity analysis of different gas species from section 4.3, makes a lack of combustion modelling an unlikely reason.

Table 4.2: Comparison of the outlet flue gas composition and the representative composition from section 2.1.1. The latter has been recalculated to ppm.

Species	Outlet composition (ppm)	Representative composition (ppm)
CO	3.3	10-60
SO_3	1.9	Few percent of SO_2
SO_2	50	90-680
KCl	227	>100
HCl	549	320-2400
O_2	51 500	70 000-140 000
H_2O	177 000	100 000-180 000
CO_2	102 000	60 000-120 000
N_2	Balance	Balance

4.4.2 The reduced chemical mechanism

Errors from the reduction of the chemical mechanism was evaluated in section 3.4.2 and was shown to have small errors in the investigated reaction region. It is possible that the tested region was too poorly resolved, which could be problematic if there were large error gradients in the reaction space.
For example in figure 3.7 the error is highest in the centre of the tested temperature region. There could also be errors outside of the investigated reaction space in the boiler. For example, the residence time was estimated on the average gas velocity of the bulk flow and a cell length of 0.05 m; the residence time may therefore have been

too small for some regions with larger cells. Further, the compositions of individual species may vary in the system, e.g. HCl. This composition was not varied during the development of the mechanism. Nonetheless, if errors with regard to varying composition was important the comparison between the reduced mechanism and full mechanism in the PFR model would most likely have shown that.

4.4.3 Homogeneous gas phase assumption

In the boiler, only homogeneous gas phase reactions are modelled and not any potential heterogeneous reactions with ash particles. Ash particles may interact with SO_3 in the form of catalysis, as mentioned in section 2.2.2. If such an effect is important it would explain the low SO_3 conversion. Incorporating the effects of ash particles into the model would be possible with known ash surface area per volume and with a reaction rate model.

4.4.4 Spray modelling

The modelling of the spray injection and vaporisation of H_2SO_4 has several uncertainties. The primary uncertainty is the interpolation error when transferring between the meshes and the neglection of vaporisation enthalpy. The interpolation error could be removed by simply solving the droplets in the same mesh as when solving the chemistry. Furthermore, droplet collision, agglomeration or breakup is not modelled; phenomena that would occur in reality. However, the impact of these errors on the SO_3 conversion and degree of sulfation are not in the right order of magnitude to change the overall results. This is due to a short residence time and therefore small changes to increase the accuracy would probably not affect the overall reaction rate.

4.4.5 Mesh

Mesh refinement was performed to achieve convergence. As a large amount of CO was injected and combusted, a large gradient of CO was created. Therefore, the CO gradient was resolved with dynamic gradient adaption. Dynamic gradient adaption was used since the reactions also were discretized with ISAT. Different ISAT tolerances lead to convergence with different mesh resolutions. The mesh was therefore refined and coarsened as the gradient of CO moved.

However, mesh independency was not explicitly fulfilled for all cases. Instead, the meshes were refined on gradients of key parameters which could have a significant impact on the conversion of SO_3. The parameters included the gradients of the molar concentration of SO_3, the magnitude of the velocity and the temperature. This meant greatly increasing the number of cells by several hundred thousand. As shown in table 4.3, a small change in the outlet concentrations of SO_3 and SO_2 was observed.

Table 4.3: Mesh refinement of the 25 000 ppm CO injection case.

Refinement	Reference	$\nabla[SO_3]$	∇T, ∇v
Mesh size	818 158	939 167	1 079 968
ppm CO out	0.94	0.95	0.90
ppm SO_3 out	142.49	142.06	146.92
ppm SO_2 out	97.85	97.86	94.73
ppm KCl out	0.038	0.038	0.038

In addition, the injection of CO caused other reactions to take place over a very short distance. If selectivity changes over a very short region then poor resolution could lead to a large error. This was investigated by refining the gradient of the reaction rate for reactions important for the sulfation process. An example was refinement on reaction 2.6 in section 2.2.1. The impact on the results was noticeable but not enough to reach the measured values. For example, the SO_3 outlet molar fraction changed from 125 ppm to 109 ppm with a change of 300 000 extra cells for the CO-H_2 injection case. Therefore, as the change in outlet concentrations was small, further refinement should not have a considerable impact on the results.

4.4.6 Discretization scheme

In the simulations, all fields except species and discrete ordinates were discretized with a second order upwind scheme. The species and the discrete ordinates were discretized with a first order upwind scheme. This was to retain the physical representation of the flow- and temperature field obtained by Sundborg and Tärnåsen [3]. The species were discretized with the first order upwind scheme in order to increase the stability of the solution. However, using a first order scheme may induce numerical diffusion, particularly if the cells are not aligned in the flow direction, as in the case of swirls in the boiler. The effect on the results was therefore studied by discretizing the species with the second order upwind scheme. A negligible effect on the results was observed, as shown in table 4.4

Table 4.4: Comparison of results for two discretization schemes, 25 000 ppm CO injection case with 818 158 cells.

Species discretization order	1st	2nd
ppm CO out	1.3	0.9
ppm SO_3 out	136.1	142.5
ppm SO_2 out	101.7	97.9
ppm KCl out	0.04	0.04
Mass imbalance (%)	1.7e-4	0.7e-4
K molar imbalance (%)	-1.7	-0.1
S molar imbalance (%)	-0.56	-0.34

4.4.7 ISAT discretization

Since the ISAT algorithm discretizes the reaction space in the form of error tolerance size, this resolution could affect the results. Therefore an ISAT discretization independent solution is desired. In theory, a lower ISAT error tolerance corresponds to a more highly resolved solution but at the expense of computational time [36]. A study was therefore conducted, where different error tolerances of ISAT were allowed, as shown in table 4.5.

Table 4.5: Comparison of different error tolerances, 25 000 ppm CO injection case with 818 158 cells.

ε_{tol}	1e-3	1e-4	1e-5
ppm CO out	1.39	1.27	1.34
ppm SO_3 out	137.23	136.04	136.13
ppm SO_2 out	100.96	101.60	101.65
ppm KCl out	0.044	0.037	0.043
K molar imbalance (%)	-1.12	-1.36	1.69
S molar imbalance (%)	-0.059	-0.061	-0.068

The study was conducted by changing the ISAT error tolerances for a solution that was converged. The reference case is therefore the solution with ε_{tol} = 1e-5. At a cell number of 818 518 cells, a change in the ISAT error tolerance did not affect the results. This implies that the solution is ISAT discretization independent.

5
Conclusion

The results presented in the previous chapter showed that there are a multitude of challenges with the CFD analysis of the sulfation process. The most notable being that the SO_3 conversion to SO_2 and the degree of sulfation were lower respective higher than the measured values.

The number of numerical errors were reduced. This included ensuring convergence of molar, mass and heat balances, removing poorly resolved gradients, evaluating the error in the reduced chemical mechanism and establishing ISAT independence. Further refinements of the mesh may be done to ensure mesh independence. However, this would most likely not have a significant effect on the overall results. There could also be an unknown error in the reduced mechanism since the resolution of the reaction space was not very high.

However, similar results in terms of the SO_3 to SO_2 conversion was obtained in both CHEMKIN and CFD. This is an indication that the chemical model used to describe the sulfation is the source of the problem and not any numerical problem in the CFD. It also shows that the error is not sensitive to the chemical mixing since the CHEMKIN simulation is a 1D model. Further, increasing the CO level or the temperature increases the SO_3 to SO_2 conversion.

The global mechanism was based on a least square fit against concentration profiles of SO_3 and SO_2 in a CHEMKIN PFR with CO injection. The profiles cover a small part of the possible reaction space, which means that it is reliable in narrow region. The model parameters produced a SO_3 to SO_2 ratio closer to the experimental results but with a slightly improved but still significantly overestimated sulfation. Therefore these parameters should not be used "as-is" but could possibly be improved with the addition of thermodynamic limitations or finite-rate parameters for the sulfation reaction. This could enhance the accuracy of the model with respect to sulfation process.

Still, the model could be further developed where one alternative would be the addition of catalysing fly ash particles and simulating the chemistry. In addition, evaluating other mechanisms for the SO_3 to SO_2 conversion in this system would be of interest.

Bibliography

[1] Andersson S, Blomqvist EW, Bäfver L, Jones F, Davidsson K, Froitzheim J, et al. Sulfur recirculation for increased electricity production in Waste-to-Energy plants. Waste Management. 2014;34(1):67 – 78. Available from: http://www.sciencedirect.com/science/article/pii/S0956053X13004054.

[2] Andersson S, Dolores Paz M, Phother-Simon J, Jonsson T. High temperature corrosion and dioxin abatement using sulfur recirculation in a waste-to-energy plant. In: 7th International Symposium on Energy from Biomass and Waste (2018). CISA; 2018. .

[3] Sundborg O, Tärnåsen A. Sulfating of Alkali Chlorides in Waste-to-Energy; 2018. Available from: http://studentarbeten.chalmers.se/publication/256255-sulfating-of-alkali-chlorides-in-waste-to-energy.

[4] Branchini L. In: Waste-to-Energy. Cham: Springer International Publishing; 2015. p. 19–36. Available from: https://doi.org/10.1007/978-3-319-13608-0_3.

[5] Karlsson S, Pettersson J, Johansson LG, Svensson JE. Alkali Induced High Temperature Corrosion of Stainless Steel: The Influence of NaCl, KCl and CaCl2. Oxidation of Metals. 2012 Aug;78(1):83–102. Available from: https://doi.org/10.1007/s11085-012-9293-7.

[6] Nordin A. Chemical elemental characteristics of biomass fuels. Biomass and Bioenergy. 1994;6(5):339 – 347. Available from: http://www.sciencedirect.com/science/article/pii/0961953494E0031M.

[7] Zevenhoven R, Kilpinen P. 2. In: Control of Pollutants in Flue Gases and Fuel Gases; 2005. p. 1–12.

[8] Hindiyarti L, Frandsen F, Livbjerg H, Glarborg P, Marshall P. An exploratory study of alkali sulfate aerosol formation during biomass combustion. Fuel. 2008;87(8):1591 – 1600. Available from: http://www.sciencedirect.com/science/article/pii/S0016236107004024.

[9] Glarborg P, Marshall P. Mechanism and modeling of the formation of gaseous alkali sulfates. Combustion and Flame. 2005;141(1):22 – 39. Available from: http://www.sciencedirect.com/science/article/pii/S0010218004001786.

[10] Mortensen M, Hashemi H, Wu H, Glarborg P. Modeling Post-Flame Sulfation of KCl and KOH in Bio-Dust Combustion With Full and Simplified Mechanisms. MCS11, 11th Mediterranean Combustion Symposium. 2019;.

[11] Allgurén T. Chemical interactions between potassium, nitrogen, sulfur and carbon monoxide in suspension-fired systems. PhD thesis. Chalmers University of Technology; 2017. Available from: http://proxy.lib.chalmers.se/login?url=http://search.ebscohost.com/login.aspx?direct=true&db=cat06296a&AN=clc.b2438641&site=eds-live&scope=site.

[12] Iisa K, Lu Y, Salmenoja K. Sulfation of Potassium Chloride at Combustion Conditions. Energy & Fuels. 1999;13(6):1184–1190. Available from: https://doi.org/10.1021/ef990057a.

[13] Jørgensen TL, Livbjerg H, Glarborg P. Homogeneous and heterogeneously catalyzed oxidation of SO2. Chemical Engineering Science. 2007;62(16):4496 – 4499. Available from: http://www.sciencedirect.com/science/article/pii/S0009250907004149.

[14] Hindiyarti L, Glarborg P, Marshall P. Reactions of SO3 with the O/H Radical Pool under Combustion Conditions. The Journal of Physical Chemistry A. 2007;111(19):3984–3991. PMID: 17388335. Available from: https://doi.org/10.1021/jp067499p.

[15] Lu T, Law CK. Linear time reduction of large kinetic mechanisms with directed relation graph: n-Heptane and iso-octane. Combustion and Flame. 2006;144(1):24 – 36. Available from: http://www.sciencedirect.com/science/article/pii/S0010218005001720.

[16] Pepiot-Desjardins P, Pitsch H. An efficient error-propagation-based reduction method for large chemical kinetic mechanisms. Combustion and Flame. 2008;154(1):67 – 81. Available from: http://www.sciencedirect.com/science/article/pii/S0010218007003264.

[17] Niemeyer KE, Sung CJ, Raju MP. Skeletal mechanism generation for surrogate fuels using directed relation graph with error propagation and sensitivity analysis. Combustion and Flame. 2010;157(9):1760 – 1770. Available from: http://www.sciencedirect.com/science/article/pii/S0010218010000039.

[18] ANSYS Inc. ANSYS Chemkin-Pro Reaction Workbench Manual; 2017.

[19] Andersson S, Karlsson M, Hunsinger H. Sulphur Recirculation for Low-corrosion Waste-to-Energy. In: ISWA World Congress. Hamburg; 2010. .

[20] ANSYS Inc. ANSYS Fluent Theory Guide; 2017.

[21] Chui EH, Raithby GD. Computation of Radiant Heat Transfer on a Nonorthogonal Mesh Using the Finite-Volume Method. Numerical Heat Transfer, Part B: Fundamentals. 1993;23(3):269–288. Available from: https://doi.org/10.1080/10407799308914901.

[22] Morsi SA, Alexander AJ. An investigation of particle trajectories in two-phase flow systems. Journal of Fluid Mechanics. 1972;55(2):193–208.

[23] Gran IR, Magnussen BF. A Numerical Study of a Bluff-Body Stabilized Diffusion Flame. Part 2. Influence of Combustion Modeling And Finite-Rate Chemistry. Combustion Science and Technology. 1996;119(1-6):191–217. Available from: https://doi.org/10.1080/00102209608951999.

[24] ANSYS Inc. The Generalized Finite-Rate Formulation for Reaction Modeling; 2009. [Online; available 05-April-2019]. http://www.afs.enea.it/project/neptunius/docs/fluent/html/th/node129.htm.

[25] Kjäldman L, Brink A, Hupa M. Micro Mixing Time in the Eddy Dissipation Concept. Combustion Science and Technology. 2000;154(1):207–227. Available from: https://doi.org/10.1080/00102200008947277.

[26] Bösenhofer M, Wartha EM, Jordan C, Harasek M. The Eddy Dissipation Concept—Analysis of Different Fine Structure Treatments for Classical Combus-

tion. Energies. 2018 Jul;11(7):1902. Available from: http://dx.doi.org/10.3390/en11071902.

[27] Lu L, Pope SB. An improved algorithm for in situ adaptive tabulation. Journal of Computational Physics. 2009;228(2):361 – 386. Available from: http://www.sciencedirect.com/science/article/pii/S002199910800483X.

[28] Pope SB. Computationally efficient implementation of combustion chemistry using in situ adaptive tabulation. Combustion Theory and Modelling. 1997;1(1):41–63. Available from: https://doi.org/10.1080/713665229.

[29] Andersson B, Andersson R, Håkansson L, Mortensen M, Sudiyo R, van Wachem B. Computational Fluid Dynamics for Engineers. Cambridge University Press; 2011.

[30] Johansson R, Leckner B, Andersson K, Johnsson F. Account for variations in the H2O to CO2 molar ratio when modelling gaseous radiative heat transfer with the weighted-sum-of-grey-gases model. Combustion and Flame. 2011;158(5):893 – 901. Available from: http://www.sciencedirect.com/science/article/pii/S0010218011000423.

[31] Engineeringtoolbox. Surface Tension of Water in Contact with Air; 2004. [Online; accessed 21-May-2019]. https://www.engineeringtoolbox.com/water-surface-tension-d_597.html.

[32] Rhodes FH, Barbour CB. The Viscosities of Mixtures of Sulfuric Acid and Water. Industrial & Engineering Chemistry. 1923;15(8):850–852. Available from: https://doi.org/10.1021/ie50164a033.

[33] Young TF, Grinstead SR. The Surface Tensions of Aqueous Sulfuric Acid Solutions. Annals of the New York Academy of Sciences. 1949;51(4):765–780. Available from: https://nyaspubs.onlinelibrary.wiley.com/doi/abs/10.1111/j.1749-6632.1949.tb27304.x.

[34] Internetchemie. Dichtetabelle Schwefelsäure; 2017. [Online; available 21-May-2019]. https://www.internetchemie.info/chemie-lexikon/daten/s/schwefelsaeure-dichtetabelle.php.

[35] Hirahara H, Kawahashi M. Experimental investigation of viscous effects upon a breakup of droplets in high-speed air flow. Experiments in Fluids. 1992 Oct;13(6):423–428. Available from: https://doi.org/10.1007/BF00223250.

[36] ANSYS Inc. ANSYS Fluent User's Guide; 2017.

[37] Ancuţa-Carmen M. Conversion of sulfuric acid to sulfur dioxide. Babeş-Bolyai University Cluj-Napoca; 2015.

[38] Green DW, Perry RH. McGraw Hill Professional, Access Engineering; 2008. Available from: https://www.accessengineeringlibrary.com:443/browse/perrys-chemical-engineers-handbook-eighth-edition/p200139d89972_80001.

A

Appendix

A.1 Sulfuric acid vapour pressure polynomials

The polynomials described in section 3.3.2 are presented below:

$$\begin{aligned} P_{SO_3}(Bar) = exp(&-67 + 0.2984 * T - 0.05988 * x_{H2SO4(\%)} - 0.0007424 * T^2 + \\ &0.0002116 * T * x_{H2SO4(\%)} + 0.01137 * x^2_{H2SO4(\%)} + \\ &8.066e{-}07 * T^3 + 2.866e{-}06 * T^2 * x_{H2SO4(\%)} \\ &-2.854e{-}05 * T * x^2_{H2SO4} - 0.0001242 * x^3_{H2SO4(\%)} - \\ &4.339e{-}09 * T^3 * x_{H2SO4(\%)} + 1.159e{-}08 * T^2 * x^2_{H2SO4(\%)} \\ &+1.052e{-}07 * T * x^3_{H2SO4(\%)} + 6.114e{-}07 * x^4_{H2SO4(\%)}) \end{aligned} \tag{A.1}$$

$$\begin{aligned} P_{H_2SO_4}(Bar) = exp(&-51.31 + 0.2274 * T + 0.2956 * x_{H2SO4(\%)} - 0.00058 * T^2 \\ &+7.874e{-}05 * T * x_{H2SO4(\%)} - 0.002955 * x^2_{H2SO4(\%)} + \\ &6.117e{-}07 * T^3 + 2.907e{-}06 * T^2 * x_{H2SO4(\%)} - \\ &2.594e{-}05 * T * x^2_{H2SO4(\%)} + 8.703e{-}05 * x^3_{H2SO4(\%)} - \\ &2.881e{-}09 * T^3 * x_{H2SO4(\%)} - 7.916e{-}10 * T^2 * x^2_{H2SO4(\%)} + \\ &1.424e{-}07 * T * x^3_{H2SO4(\%)} - 5.534e{-}07 * x^4_{H2SO4(\%)}) \end{aligned} \tag{A.2}$$

$$\begin{aligned} P_{H_2O}(Bar) = exp(&-3.328 + 0.06525 * T - 0.1762 * x_{H2SO4(\%)} - 0.000181 * T^2 \\ &-2.064e{-}5 * T * x_{H2SO4(\%)} + 0.004635 * x^2_{H2SO4(\%)} + \\ &2.476e{-}7 * T^3 - 6.915e{-}7 * T^2 * x_{H2SO4(\%)} + \\ &4.639e{-}06 * T * x^2_{H2SO4(\%)} - 4.526e{-}5 * x^3_{H2SO4(\%)}) \end{aligned} \tag{A.3}$$

A.2 Results from the CFD simulations

Table A.1: Results from the CFD simulations.

Simulation	Base	200ppm	25000ppm	75000ppm	321000ppm	$CO\&H_2$	Global Mech.	Measured
ppm CO out	0.1	0.61	1.3	1.4	2.1	2.8	N/A	3.1
ppm SO_2 out	52.3	59.8	101.7	107.4	112.4	120.6	260.8	220
ppm SO_3 out	189.6	170.0	136.1	121.9	125.3	109.7	1.1	2
DoS (%)	102.0	99.4	99.5	103.7	99.8	101.9	92.7	70
SO_3/SO_2 mass ratio (%)	452.9	355.3	167.3	141.7	139.2	113.3	0.5	1.5
K molar imbalance (%)	-2.05	-1.94	-1.69	-5.36	-2.60	-4.54	0.00	N/A
S molar imbalance (%)	-0.97	-0.14	-0.07	-0.84	-0.43	-0.37	0.00	N/A
Cl molar imbalance (%)	-1.16	-1.00	-0.86	-2.59	-1.16	-2.24	0.00	N/A
O molar imbalance (%)	0.00	0.00	0.00	-0.01	-0.02	-0.01	0.00	N/A
H molar imbalance (%)	0.07	0.06	0.06	0.05	0.04	0.07	0.00	N/A
C molar imbalance (%)	0.00	-0.00	0.00	-0.01	0.02	-0.08	0.00	N/A
N molar imbalance (%)	0.97	0.97	0.98	0.99	0.98	0.99	0.97	N/A
Mass imbalance (%)	9.39e-5	9.39e-5	1.62e-4	5.6e-4	6.4e-4	5.98e-5	-6.83e-5	N/A
Energy imbalance (%)	-3.11	-3.11	-3.11	-3.11	-3.11	-3.11	-3.11	N/A